JOURNAL OF GEOPHYSICAL RESEARCH, VOL. 111, B08309, doi:10.1029/2005JB004095, 2006

Statistical properties of seismic anisotropy predicted by upper mantle geodynamic models

Thorsten W. Becker,[1] Sebastien Chevrot,[2] Vera Schulte-Pelkum,[3] and Donna K. Blackman[4]

Received 8 October 2005; revised 3 April 2006; accepted 10 May 2006; published 24 August 2006.

[1] We study how numerically predicted seismic anisotropy in the upper mantle is affected by several common assumptions about the rheology of the convecting mantle and deformation-induced lattice preferred orientations (LPO) of minerals. We also use these global circulation and texturing models to investigate what bias may be introduced by assumptions about the symmetry of the elastic tensor for anisotropic mineral assemblages. Maps of elasticity tensor statistics are computed to evaluate symmetry simplifications commonly employed in seismological and geodynamic models. We show that most of the anisotropy predicted by our convection-LPO models is captured by estimates based on a best fitting hexagonal symmetry tensor derived from the full elastic tensors for the computed olivine:enstatite LPOs. However, the commonly employed elliptical approximation does not hold in general. The orientations of the best fitting hexagonal symmetry axes are generally very close to those predicted for finite strain axes. Correlations between hexagonal anisotropy parameters for *P* and *S* waves show simple, bilinear relationships. Such relationships can reduce the number of free parameters for seismic inversions if this information is included a priori. The match between our model predictions and observed patterns of anisotropy supports earlier, more idealized studies that assumed laboratory-derived mineral physics theories and seismic measurements of anisotropy could be applied to study mantle dynamics. The match is evident both in agreement between predicted LPO at selected model sites and that measured in natural samples, and in the global pattern of fast seismic wave propagation directions.

Citation: Becker, T. W., S. Chevrot, V. Schulte-Pelkum, and D. K. Blackman (2006), Statistical properties of seismic anisotropy predicted by upper mantle geodynamic models, *J. Geophys. Res.*, *111*, B08309, doi:10.1029/2005JB004095.

1. Introduction

[2] Many regions within the upper ~400 km of the mantle are seismically anisotropic [e.g., *Hess*, 1964; *Forsyth*, 1975; *Anderson and Dziewoñski*, 1982; *Vinnik et al.*, 1989; *Montagner and Tanimoto*, 1991], but the symmetry class, patterns, and length scales of anisotropy variations remain debated. Partly, this is due to insufficient data coverage for both body and surface waves. Trade-offs between model parameters such as isotropic and anisotropic structure complicate seismic inversions further [e.g., *Tanimoto and Anderson*, 1985; *Laske and Masters*, 1998]. Understanding anisotropy, however, may hold the key for unraveling the evolution of surface tectonics and constraining mantle flow. We thus present new geodynamic models to strengthen the connection between synthetic and observed anisotropy. By combining global mantle flow and mineral physics modeling, we are able to produce realistic synthetic anisotropy maps, which we analyze with regard to their statistical properties in order to guide future seismological inversions.

[3] We are only concerned with subcrustal anisotropy, and do not discuss the potentially complicating nature of the crust, or the existence of anisotropy in deeper regions of the Earth. Upper mantle anisotropy is most likely due to lattice preferred orientation (LPO) of intrinsically anisotropic crystals under dislocation creep [e.g., *Nicolas and Christensen*, 1987; *Karato*, 1992; *Mainprice et al.*, 2000]. Under progressive deformation, the crystallographic axes corresponding to fast seismic velocities (*a* [100] for olivine) may align with the largest axis of the finite strain ellipsoid (FSE) [e.g., *McKenzie*, 1979; *Wenk et al.*, 1991; *Ribe*, 1992; *Ben Ismail and Mainprice*, 1998] or rotate further into the shear plane [e.g., *Zhang and Karato*, 1995; *Jung and Karato*, 2001; *Wenk and Tomé*, 1999; *Kaminski and Ribe*, 2001, 2002; *Katayama et al.*, 2004]. Given this connection between LPO and rock deformation, numerous attempts have

[1]Department of Earth Sciences, University of Southern California, Los Angeles, California, USA.
[2]Laboratoire de Dynamique Terrestre et Planétaire, UMR 5562, Observatoire Midi-Pyrénées, Université Paul Sabatier, Toulouse, France.
[3]Department of Geological Sciences, CIRES, Boulder, Colorado, USA.
[4]Institute of Geophysics and Planetary Physics, Scripps Institution of Oceanography, University of California, San Diego, La Jolla, California, USA.

0148-0227/06/2005JB004095$09.00

been made to link anisotropy with plate tectonic motion and mantle flow. Idealized convection settings have been addressed [e.g., *Ribe*, 1989; *Chastel et al.*, 1993; *Tommasi*, 1998; *Tommasi et al.*, 1999; *Blackman and Kendall*, 2002], specific regions have been modeled with varying degree of realism [e.g., *Russo and Silver*, 1994; *Hall et al.*, 2000; *Silver and Holt*, 2002; *Becker*, 2002; *Gaboret et al.*, 2003; *Behn et al.*, 2004], and global comparisons of predicted and observed anisotropy have been made [*Becker et al.*, 2003].

[4] Recent work evaluates some of the simplifying assumptions in the idealized models. Initial results show that the main conclusions of previous workers are confirmed even for more sophisticated treatments of anisotropy and mantle rheology [*Becker et al.*, 2004; *Čadek*, 2005]. Here, we continue the process of evaluation, this time using the kinematic theory of *Kaminski and Ribe* [2001] to estimate LPO predictions of global mantle circulation models, and to derive novel forward models of seismic anisotropy in a statistical sense. Using LPO-derived anisotropy allows a direct link with seismology in terms of anisotropy strength. Our goal is to determine how much of the anisotropy is of hexagonal character, and whether correlations between hexagonal anisotropy parameters exist so that seismological inversion can be simplified. This work is in line with previous attempts to constrain the radial distribution of anisotropy of the upper mantle based on laboratory measurements, natural samples, and seismology [*Estey and Douglas*, 1986; *Montagner and Nataf*, 1988; *Montagner and Anderson*, 1989; *Montagner and Guillot*, 2000] as well as geodynamic a priori models for isotropic structure such as 3SMAC [*Nataf and Ricard*, 1996].

[5] The modeling employed to study convection, texturing and effective elastic structure each depend on assumptions and/or parameter values so we review our methods briefly, in some cases providing further detail in the appendices. Results are presented first in a set of examples that illustrate predicted LPO within the global circulation model. Then we analyze global statistical anisotropy properties. Most of the predicted upper mantle anisotropy is of hexagonal character, and the best fitting fast axes from LPO align with the largest FSE axes in most places. Our previous conclusions about the general character of upper mantle anisotropy from flow are thus confirmed with more sophisticated models. Moreover, the variability of synthetic LPO fabrics matches that of natural samples, lending credibility to the correlations that we show exist between hexagonal anisotropy parameters used for seismological inversions.

2. Methods

2.1. Mantle Flow Modeling

[6] We use a global mantle flow modeling approach of the type that can explain a range of geophysical observables, as has been shown over the last two decades. Following *Becker et al.* [2003], surface plate motions are prescribed and density distribution is inferred from the SMEAN average tomography model [*Becker and Boschi*, 2002]. A constant factor is used to convert this seismic model to density: $R = d \ln \rho / d \ln v_S$, where ρ is density and v_S shear wave velocity. Density shallower than 220 km is set to zero in cratonic regions (from 3SMAC) to avoid compositional effects in the tectosphere. Geodynamic model parameters are given in Table 1. Values used were previously found to lead to force equilibrium [*Becker and O'Connell*, 2001] and a good match of predicted FSE orientations to observed azimuthal anisotropy based on Rayleigh waves [*Becker et al.*, 2003].

Table 1. Geodynamic Model Parameters

Parameter	Symbol	Value
Density scaling	$R = d \ln \rho / d \ln v_S$	0.15
Nondimensionalized temperature	T	
Temperature scaling	$d \ln T / d \ln v_S$	−4.2
Rayleigh number[a]	Ra	1.5×10^8
Reference viscosity	η_0	10^{21} Pa s
Activation energy[b]	E	30

[a]As defined by *Zhong et al.* [2000], based on Earth radius.
[b]Normalized and nondimensionalized as in the simplified temperature-dependent viscosity law equation (A1).

[7] The buoyancy forces due to the imposed density structure of the mantle have a strong effect on the flow. We have chosen R = const for simplicity, but in reality, both depth dependence or R and compositional effects may affect the flow. We consider SMEAN to be a viable best guess for the large-scale (spherical harmonic degree $\ell \sim 30$) tomographic structure of the mantle [e.g., *Becker et al.*, 2003; *Niehuus and Schmeling*, 2005].

[8] The equations for instantaneous, incompressible, and infinite Prandtl number flow are solved using the semi-analytical method of *Hager and O'Connell* [1981] for the reference models with only radially varying viscosity. The radial viscosity, η_0, of the reference models is a generic profile [*Hager and Clayton*, 1989] with $\eta_0 = 50$ (depths $z <$ 100 km), $\eta_0 = 0.1$ (100 km $\leq z <$ 410 km), $\eta_0 = 1$ (410 km $\leq z <$ 660 km), and $\eta_0 = 50$ for $z \geq$ 660 km, in units of 10^{21} Pa s. This profile, η_D, leads to azimuthal anisotropy model fits almost as good as those of more complicated profiles. In the subsequent sections we mainly refer to the results for the reference model but we also explored models with laterally varying viscosity (see Appendix A). Such models displayed regionally modified velocity fields, mainly due to the differences in suboceanic and continental viscosity. On average, however, model fits to surface wave anisotropy were comparable to our reference model and anisotropy strength statistics, on which we focus here, were quite similar.

[9] The mantle flow is assumed to be steady state. This could be a limitation if long advection times are required for the development of LPO. In general, our models may be expected to be most applicable to oceanic regions, which behave in a simpler fashion than continental ones. There, past tectonic episodes may strongly affect seismic anisotropy in a thick, old crust and lithosphere. In contrast to *Čadek*'s [2005] models, we consistently find better model fits when limiting comparison with anisotropy to oceanic plates [*Becker et al.*, 2003].

2.2. LPO for Olivine-Enstatite Assemblages

[10] We compute LPO following the kinematic theory of Kaminski and Ribe [2001, 2002] (hereinafter referred to as KR). With this extension of earlier work by *Ribe and Yu* [1991] and *Ribe* [1992], it is possible to account for recrystallization effects, where the highest density of olivine [100] axes is observed to rotate away from the direction of

maximum extension described by the FSE [*Zhang and Karato*, 1995; *Zhang et al.*, 2000]. The KR method is computationally faster than alternative, physically more consistent descriptions of fabric development such as the VPSC approach [*Wenk et al.*, 1991; *Wenk and Tomé*, 1999]. However, results from different fabric theories are expected to be similar for our large-scale, low-resolution flow models [*Tommasi*, 1998; *Blackman et al.*, 2002; *Blackman and Kendall*, 2002]. The KR method addresses a range of laboratory findings for LPO development [*Kaminski and Ribe*, 2002]. We shall assume dominance of low water/stress, ''classic'', A-type (in the nomenclature of *Jung and Karato* [2001]) slip systems throughout the upper 410 km of the mantle for simplicity. All parameters for the KR method are chosen as by *Kaminski et al.* [2004]. This means that we are attempting to account for dynamic recrystallization, grain boundary migration, and we are generally using a 70% olivine (ol)/30% enstatite (en) mineral assemblage.

[11] We use the D-REX implementation of the KR method [*Kaminski et al.*, 2004] with ~2200 virtual grains, whose assemblage deformation is modeled by incorporating velocity gradients along streamlines. We compute these particle paths by advecting tracers using a step-size controlled Runge-Kutta method with polynomial velocity interpolation as described by *Becker et al.* [2003]. D-REX provides time derivatives of the direction cosines describing grain orientations and orientation density functions. We found that limiting the maximum integration time step to <0.01 of a characteristic timescale (given by the inverse of the maximum strain rate) yielded stable results (smaller than 0.1% deviation in best fit transverse isotropy, TI, orientations with respect to time step refinement). There is some sensitivity of predicted LPO to the spatial resolution of the velocity (mantle flow) model. However, for our global, low-resolution flow model (up to spherical harmonic degrees $\ell \sim 30$ and $\ell \sim 60$ for density and surface velocities, respectively) we found that results were not strongly dependent on the interpolation method; refining our standard ~50 km spacing of grid cells further led to very similar results [*Becker et al.*, 2003]. As we neglect the potential feedback of LPO on modifying the flow, we can treat convection and LPO models separately, which expedites the computations.

[12] Following *Ribe* [1992] and *Becker et al.* [2003], we advect tracers and let LPO develop along the path until the logarithmic saturation strain, ξ_c, defined as the maximum of

$$\xi = \log(e_1/e_2) \qquad \zeta = \log(e_2/e_3), \tag{1}$$

has reached a critical value of $\xi_c = 0.5-2$ (see also Appendix B). Here, e_1, e_2, and e_3 are the largest, intermediate, and smallest eigenvalue of the FSE, respectively. Tracers arrive with random LPO from below 410 km depth, as the phase transition there likely erases fabrics. We also employ a maximum advection time of 60 Ma, to not overstretch the assumption of stationary flow.

2.3. Elastic Anisotropy and Seismic Interpretation

[13] At every location where we wish to predict anisotropy, we estimate an effective elasticity tensor, C, for the grain assemblage using single-crystal (SC) elasticity constants and the orientation distribution. The best averaging procedure for anisotropic assemblages is still debated. The *Voigt* [1928] approach assumes constant strain in the averaging volume (which may be appropriate for seismic waves sampling the medium) and will result in an upper bound on anisotropy amplitudes. Alternatively, *Reuss* [1929] (constant stress) averaging will predict a lower bound. We found that Reuss estimates of anisotropy as expressed as elastic tensor norms are ~5% lower than the Voigt estimates. (Tensor norm anomalies as quoted here are ~2 times the expected seismic velocity variations.) Anisotropy orientation patterns (e.g., best fit TI axes orientations) were very similar between the two averaging approaches, however. As discussed by [*Mainprice et al.*, 2000], measured velocities for upper mantle rocks are typically within 5% of the Voigt average [e.g., *Barruol and Kern*, 1996], and only Voigt averaging is consistent with the tensor decomposition method of *Browaeys and Chevrot* [2004] which we shall employ. Therefore mostly Voigt averaging results are reported here.

[14] For general anisotropy, 21 components of C are independent, but inversions cannot reliably determine all of them from seismological data alone. It is also not clear to what extent complex anisotropy is realized in the Earth. Several simplifications have therefore been applied for inversions [e.g., *Silver*, 1996; *Montagner and Guillot*, 2000], and often hexagonal symmetry has been assumed. Such anisotropy has one symmetry axis which typically, but not always, corresponds to the direction of fastest propagation. Hexagonal symmetry axes are aligned in the vertical or horizontal plane for the special cases of radial and azimuthal anisotropy, respectively. Once we estimate C, it is therefore of interest to also evaluate the best fitting hexagonal anisotropy, C^h. We determine C^h at each location from the sum of isotropic, $\tilde{C}^{\mathrm{iso}}$, and hexagonal component projections, $\tilde{C}^{\mathrm{hex}}$, of C,

$$C^h = \tilde{C}^{\mathrm{iso}} + \tilde{C}^{\mathrm{hex}}. \tag{2}$$

These projections are computed using the method of *Browaeys and Chevrot* [2004].

[15] Elements of C^h may be rewritten in various notations, e.g., that of *Love* [1927]. Here, we choose to focus on the commonly used $\{\varepsilon, \gamma, \delta\}$ parameters:

$$\text{P anisotropy} \quad \varepsilon = \frac{C^h_{11} - C^h_{33}}{2\bar{C}_{11}}, \tag{3}$$

$$\text{S anisotropy} \quad \gamma = \frac{C^h_{66} - C^h_{44}}{2\bar{C}_{44}}, \tag{4}$$

$$\text{Ellipticity} \quad \delta = \frac{C^h_{13} - C^h_{33} + 2C^h_{44}}{\bar{C}_{11}}, \tag{5}$$

where

$$\bar{C}_{11} = \langle \tilde{C}^{\mathrm{iso}}_{11} \rangle = \bar{v}_P^2 \rho, \tag{6}$$

$$\bar{C}_{44} = \langle \tilde{C}^{\mathrm{iso}}_{44} \rangle = \bar{v}_S^2 \rho. \tag{7}$$

Here, $C = C_{ij}$ is written as a (6, 6) Voigt matrix using the standard tensor nomenclature [e.g., *Browaeys and Chevrot*, 2004]. Often, $\varepsilon - \delta = 0$ is assumed for simplicity, this special case is called elliptical anisotropy. The reference values for the isotropic $\bar{C}_{11}$ and $\bar{C}_{44}$ are related to the *P* and *S* wave velocities, $\check{v}_P$ and $\check{v}_S$, as indicated; they are obtained by a global, lateral layer average of the respective components of the isotropic projection, $\tilde{C}_{11}^{\mathrm{iso}}$ and $\tilde{C}_{44}^{\mathrm{iso}}$, denoted by $\langle\rangle$. Using *Estey and Douglas*'s [1986] SC parameters, $\check{v}_S$ and $\check{v}_P$ match PREM values to within 1% on average for depths >30 km. If we use the corresponding mean hexagonal values $\tilde{C}_{11}^{\mathrm{iso}} \approx (C_{11}^h + C_{33}^h)/2$ and $\tilde{C}_{44}^{\mathrm{iso}} \approx (C_{44}^h + C_{66}^h)/2$ instead, velocities deviate from PREM by less than 4%. To find the *P* and *S* wave hexagonal anisotropy parameters (equations (3)–(5)), we decompose each elastic tensor into its symmetry components in a rotated hexagonal, Cartesian symmetry system [*Browaeys and Chevrot*, 2004]. This procedure achieves a characterization of tensor complexity and seismic properties that is independent of the coordinate system. This is a significant simplifying advantage over earlier attempts that have additionally explored possible rotations of tensors [*Montagner and Anderson*, 1989].

[16] Elasticity tensors for olivine and enstatite (orthopyroxene) single crystals as well as their dependence on temperature, *T*, and pressure, *p*, (only linear derivatives) were generally taken from the compilation of *Estey and Douglas* [1986]. We also use more up-to-date lab measurements: for olivine, the reference values and pressure derivatives are from *Abramson et al.* [1997], and the temperature derivative is from *Isaak* [1992] (RAM sample). For enstatite, the reference and pressure derivative are from *Chai et al.* [1997] ($En_{0.80}Fs_{0.20}$). A one-dimensional (1-D) temperature and pressure profile applies so that *p*, *T* change only as a function of depth, and so modify the SC tensors before averaging at each tracer location. The thermal depth profile is (simplified) from *Stacey* [1977], and *p* (without crustal layer) from PREM [*Dziewoski and Anderson*, 1981] (see Figure 1a). These choices were made for simplicity and consistency with *Browaeys and Chevrot* [2004], more elaborate *p*, *T* models are possible. We found that orientations of predicted anisotropy are, again, much less affected by the uncertainties in *dC*/*dT* and *dC*/*dp* than amplitudes. We chose to include depth-dependent variations for increased realism. However, interpretations of anisotropy amplitudes should be made with caution given the uncertainties in the partial derivatives.

3. Results

[17] We now discuss the 1-D anisotropy properties of our model, present example LPO synthetics from selected sites within our flow computation, and then proceed to discuss global anisotropy statistics. A series of benchmark tests were run to compare predictions of anisotropy using our methods and simple strain conditions with measured anisotropy on several natural samples. We find that saturation strain values of $\xi_c = 1.5–2$ are required to achieve a reorientation of preexisting fabrics following a change in strain field. Variable strain fields will be encountered by mineral assemblages in mantle circulation, so these higher values of ξ_c may be most appropriate. Appendix B provides

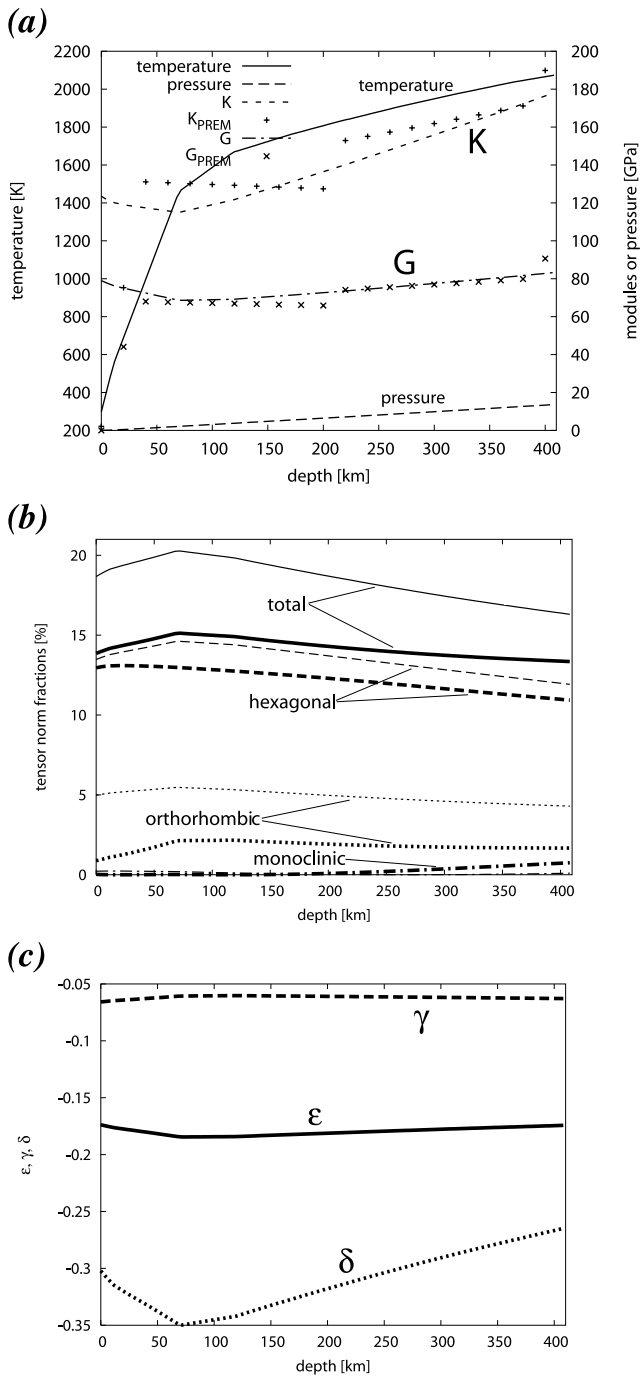

Figure 1. (a) Depth dependence of 1-D model temperature and Voigt-averaged isotropic moduli (*K*, incompressibility; *G*, shear modulus) for the reference, single-crystal mineral assemblage; elastic constants and *p*/*T* derivatives from *Estey and Douglas* [1986]. Assemblage contains 70% olivine and 30% enstatite, and [001] and [010] symmetry axes of enstatite are aligned with olivine [100] and [001], respectively. (b) Elastic tensor norm fractions (heavy lines, mineral mix; thin lines, 100% olivine), and (c) hexagonal factors (for ol/en mix, equations (3)–(5)), both as a function of depth.

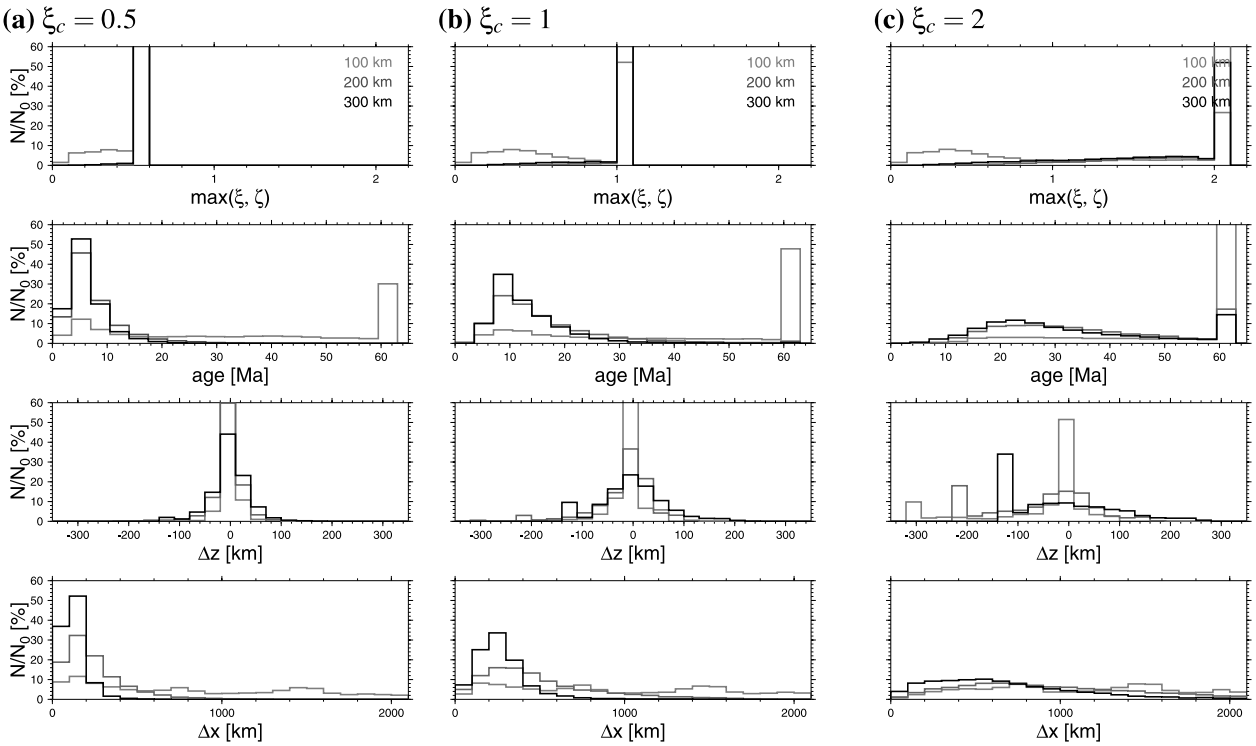

Figure 2. Effect of parameter values on behavior along tracer paths. Results for target saturation strains of (a) ξ_c = 0.5, (b) ξ_c = 1, and (c) ξ_c = 2 for the reference circulation model. Histograms for sets of globally distributed tracers ending up in layers at 100, 200, and 300 km depth (shades of gray) show (first panels) finite strain achieved by tracer end point, (second panels) corresponding advection times, and (third panels) vertical and (fourth panels) horizontal distance between advection start and endpoint.

details of the benchmark tests, explains the steps for plotting seismic characteristics at specific locations within the model space, and shows seismic characteristics for natural samples from the literature.

3.1. The 1-D Average Properties for an Unstrained, Single-Crystal Assemblage

[18] We are concerned with the average properties of seismic anisotropy in the upper mantle. Since the derivatives of the individual C components are not identical, the relative symmetry characteristics of olivine and enstatite vary as a function of depth [e.g., *Browaeys and Chevrot*, 2004]. For large strain under simple shear (and presumably mantle flow), the [001] and [010] symmetry axes of enstatite will align with olivine [100] and [001], respectively [e.g., *Kaminski et al.*, 2004]. We shall use this flow alignment when averaging SC values for reference. (In the deformation experiments and flow computations, the dynamic alignment of both olivine and enstatite grains is computed by DREX.)

[19] Figure 1 shows the depth dependence of isotropic elastic parameters compared to PREM values, and tensor symmetry fractions, respectively, using the *Estey and Douglas* [1986] estimates, Voigt averaging, and our simple lithosphere and mantle geotherm. (A similar estimate was given by *Browaeys and Chevrot* [2004], but the SC tensors of ol and en were not aligned properly there, leading to inaccuracies.) All tensor fractions cited here are in terms of the tensor norms of the respective symmetry component projection (e.g., the hexagonal part of the tensor) divided by the total tensor norm, as by *Browaeys and Chevrot* [2004]. The mean total, hexagonal, and orthorhombic anisotropy tensor norm fractions of a perfectly aligned ol (70%) + en (30%) assembly are ~14, 12, and 2%, respectively, for the upper 410 km and *Estey and Douglas* [1986] constants. Using the more recent elasticity tensor estimates, the respective fractions are ~13, 12, and 1%. These single-crystal anisotropies form an upper bound for possible anisotropy in geodynamic models.

3.2. Anisotropy From Global Models

[20] Given that required saturation strains for LPO development may be larger than previously considered (Appendix B), we start our discussion of anisotropy from global flow models by revisiting earlier estimates of typical advection times and distances [*Becker et al.*, 2003]. We show results from our reference model with steady state circulation, SMEAN tomography, and viscosity η_D. Statistical results for the actual achieved strains and other parameters for three values of ξ_c are shown in Figure 2.

[21] We observe that larger ξ_c requires long advection distances and times, so that many tracers reach the cutoff time of 60 Ma for ξ_c = 2, rather than achieving the actual desired strain. Also vertical distances traveled increase substantially for $\xi_c \gtrsim 1$, as the Δz plots in Figure 2 show. The side lobes in the histogram are due to the distance traveled from 410 km depth, where texturing is initiated. Figure 2 is of course merely a convolution of the distribution of strain rates throughout the mantle with the ξ_c requirement. Strain rates in the upper mantle are strongly

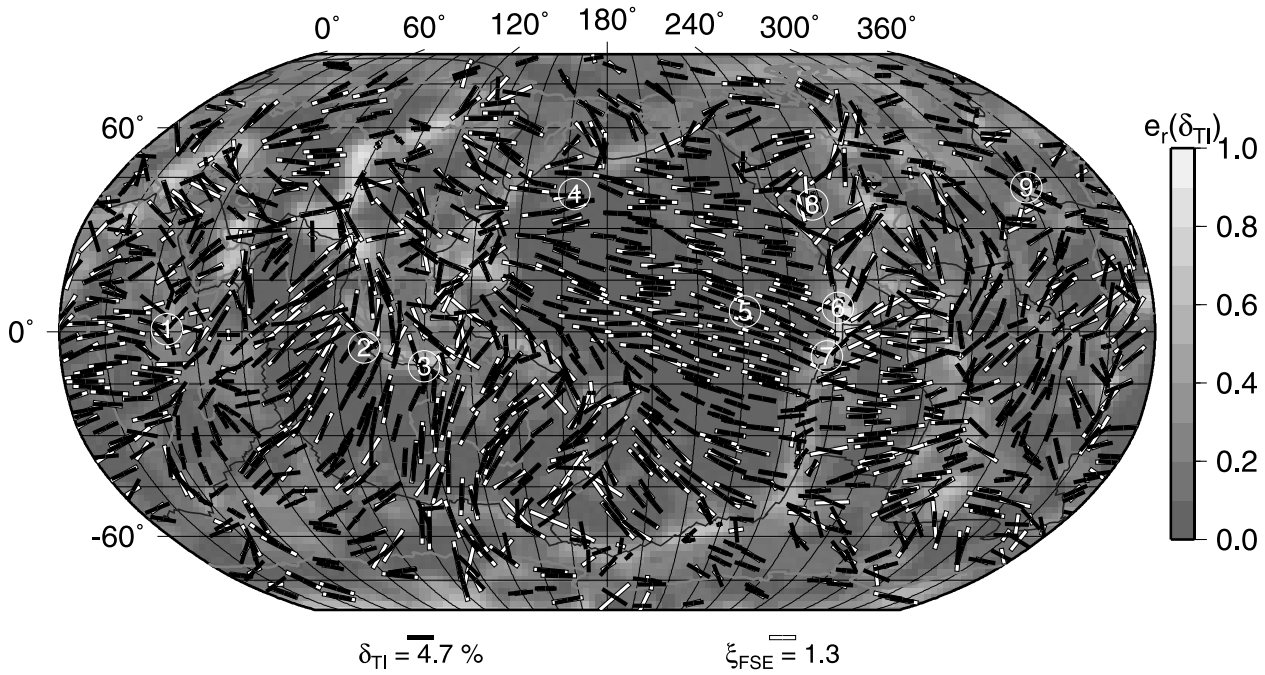

Figure 3. Comparison of predicted fast TI axis from LPO and long FSE axis orientations at 200 km depth in the reference model with $\xi_c = 2$: TI azimuth (black axes), and TI radial component (background shading; legend below plot gives $\delta v_S = 2\Delta v_S/(v_{S1} + v_{S2})$, see Appendix B), and FSE (white bars, scaled by ξ). Circled numbers denote type localities chosen for further analysis in Figures 4 and 5.

affected by the radial viscosity profile, the prescribed surface velocities, and, somewhat less so, by the distribution of buoyancy forces. Straining is slower in the stiffer lithosphere and maximum in the low η layer around 250 km. Laterally, shearing is most rapid underneath the oceanic plate regions [*Becker et al.*, 2003], as expected given the fast plate velocities there. Allowing for lateral η variations, suboceanic regions are predicted to be relatively low viscosity, both because v_S tomography is relatively slow there, and because relatively higher shear strains will reduce a power law viscosity. The upper mantle advection statistics for models with temperature-dependent ($\eta(T)$) and temperature and strain-rate-dependent viscosity ($\eta(T, \dot{\varepsilon})$, see Appendix A) look similar to Figure 2, but shearing is more rapid for these models. Mean advection times for tracers that did not reach the cutoff time at 200 km for $\xi_c = 2$ are reduced to 28 and 26 Ma for $\eta(T)$ and $\eta(T, \dot{\varepsilon})$, respectively, compared to 31 Ma for the $\eta(z)$ model, for example.

3.2.1. LPO and FSE Fast Axes

[22] Figure 3 compares the spatial patterns of azimuthal anisotropy predicted at 200 km depth, from the FSE as a proxy and from best fitting, fast symmetry TI axes, as computed from the full C tensor based on the predicted LPO. Nine example localities were selected to illustrate the variability of LPO fabrics, and Figure 4 shows pole figures for these. Variations in LPO are strongest outside regions of coherent shear such as underneath the younger parts of the Pacific plate. A comparison between FSE axes and best fit TI shows that, even for the large advection times of ξ_c, FSE orientations align with the TI axes within large geographic regions. This finding is consistent with earlier work in two dimensions [*Tommasi*, 1998; *Tommasi et al.*, 2000; *Blackman et al.*, 2002] and substantiates interpretation of seismic anisotropy using global flow models which were based on instantaneous strain rates [*Gaboret et al.*, 2003; *Behn et al.*, 2004] and FSE orientations [*Hall et al.*, 2000; *Becker et al.*, 2003].

[23] Exceptions to the match between TI and FSE are regions of strong upwelling (e.g., East African Rift), and the plate margins. The mean, area weighted, angular misfit, $\langle\Delta\alpha\rangle$, for the two approaches of predicting anisotropy is 4.9(4.1)° and 13.6(12.6)° at 200 km depth for $\xi_c = 0.5$ and $\xi_c = 2$, respectively. The numbers in parentheses are averages restricted to oceanic plate regions (from 3SMAC). (The $\Delta\alpha$ misfit is obeys $0 \leq \Delta\alpha \leq 90°$, with $\langle\Delta\alpha\rangle = 45°$ indicating randomness, no correlation.) Mean angular deviations for different approaches of estimating seismic anisotropy may be compared with the formal uncertainty in azimuthal anisotropy orientations from individual Rayleigh inversions. We estimated those to be $\sim$10° for *Ekström*'s [2001] phase velocity maps [*Becker et al.*, 2003].

[24] For $\eta(T)$ and $\eta(T, \dot{\varepsilon})$ the $\xi_c = 2$ deviations at 200 km are slightly increased to 13.8(14.1)° and 14.7(16)°, respectively. This is consistent with our results that the velocities of the laterally varying η models show more regional complexity, as it is regions of large strain rate changes along flow lines where we might expect different mineral physics theories to yield varying predictions [e.g., *Tommasi et al.*, 2000].

[25] The comparison shown in Figure 3 is equivalent to evaluating the grain orientation lag (II) parameter of *Kaminski and Ribe* [2002] which compares convective and LPO formation timescales. Our results indicate that the timescales on which mantle flow changes along a streamline are generally long compared to fabric development times. We conclude that a good match between FSE

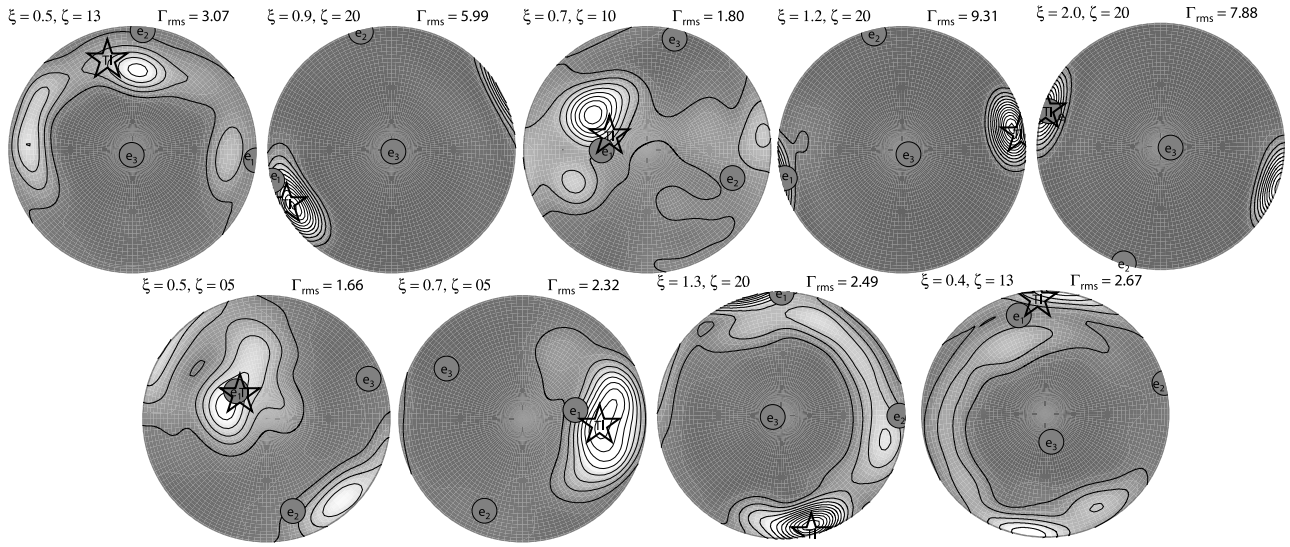

Figure 4. Pole figures of orientation density (ODF) distributions for olivine *a* [100] axes for the nine type localities shown in Figure 3, consecutive numbering left to right, top to bottom. We show upper hemisphere, equal-area projections oriented in a geographic reference frame; north and east are up and right, respectively. The title line above each plot indicates the degree of finite strain reached (ξ, ζ, equation (1)) and the RMS of the ODF (normalized to random), by which the plots are normalized for visualization purposes (isolines plotted every 0.2, bright colors indicating higher concentration of *a* axes). The e_i labels indicate the location where the principal axes of the FSE plot (e_1 corresponding to largest eigenvalue); open star denotes the orientation of the best (worst) fitting hexagonal symmetry axes for dominant fast (slow) symmetry, an approximation of the fast v_S plane.

and LPO exists on the global scale. Models that include strongly time-dependent convection and/or larger lateral viscosity contrasts may alter these conclusions, though we do not expect this to be the case for global, large-scale models.

3.2.2. Anisotropy Strength

[26] The amplitude of predicted anisotropy in our model clearly depends on the details of straining, ξ_c, and the depth dependence of *C* (Figures 1 and 4). In nature, the creation and destruction of LPO will further depend on temperature and stress conditions, and our results for anisotropy strength (e.g., δv_S, equation (B2)) are thus probably an upper bound. For our circulation models and saturation strains of $\xi_c = 2$, we predict RMS values for δv_S of 3.9, 4.3, and 4.2% at 100, 200, and 300 km, respectively. The depth dependence of these globally averaged numbers reflects relatively slow strain accumulation in the lithosphere, and proximity to the 410 km depth, fabric-erasing boundary, respectively, as expected from our advection time estimates (Figure 2). These predicted anomalies are comparable, but on the high end, to anomalies in seismological models of radial upper mantle anisotropy, e.g., ~3% RMS variations in $(v_{SH} - v_{SV})/v_S$ at 100 km depth in *Boschi and Ekström*'s [2002] model. They are much larger than RMS variations in the 2ϕ signal of azimuthal anisotropy variations (e.g., 0.6% mean and 2.5% maximum anomalies for $T = 50$ s Rayleigh waves [*Ekström*, 2001]) for the upper mantle. Anomalies of $\delta v_S \sim$ 5% correspond to shear wave splitting times of ~2.2 s for a 200 km thick layer and 5° incidence, for example, comparable to the larger observed splitting delays [e.g., *Silver*, 1996; *Savage*, 1999]. However, this comparison does not consider propagation effects in a medium with vertically [*Rümpker and Silver*, 1998; *Saltzer et al.*, 2000; *Schulte-Pelkum*, 2001] or laterally [*Favier and Chevrot*, 2003] varying anisotropy. Our initial comparisons for regional models using reflectivity seismogram modeling [cf. *Hall et al.*, 2000] show that delay times are very similar to observations [*Becker et al.*, 2006]. These findings of appropriate predictions of *SKS* splitting, but overprediction of azimuthal surface wave anisotropy may be significant. Possible reasons include overestimates of the effectiveness of dislocation creep [cf. *McNamara et al.*, 2003] or of the dominance of A-type slip systems [cf. *Mainprice et al.*, 2005]. However, the amplitude mismatch may also be related to the fact that phase velocity maps involve more indirect, inversion-based estimates than splitting. Especially if there are large lateral variations in the fast propagation planes (as may be expected given detailed *SKS* studies [e.g., *Fouch et al.*, 2004]), surface wave models may underpredict anisotropy strengths. This highlights the need to further evaluate comparisons between different seismological estimates of anisotropy [e.g., *Montagner et al.*, 2000; *Becker*, 2002; *Simons and van der Hilst*, 2003] using more sophisticated mineral physics and geodynamic models.

3.2.3. LPO Variations in Nature and Synthetics

[27] We now evaluate the degree of complexity in seismic anisotropy predicted by our large-scale geodynamic models. Figure 5 shows the estimated shear wave anisotropy for the type localities that correspond to the poles in Figure 4. These are not meant as detailed predictions for specific locations on Earth, but rather as typical examples that may reflect the general plate tectonic setting. Using the best fit hexagonal anisotropy reference frame and depth-dependent *C* following *Estey and Douglas* [1986], these plots show

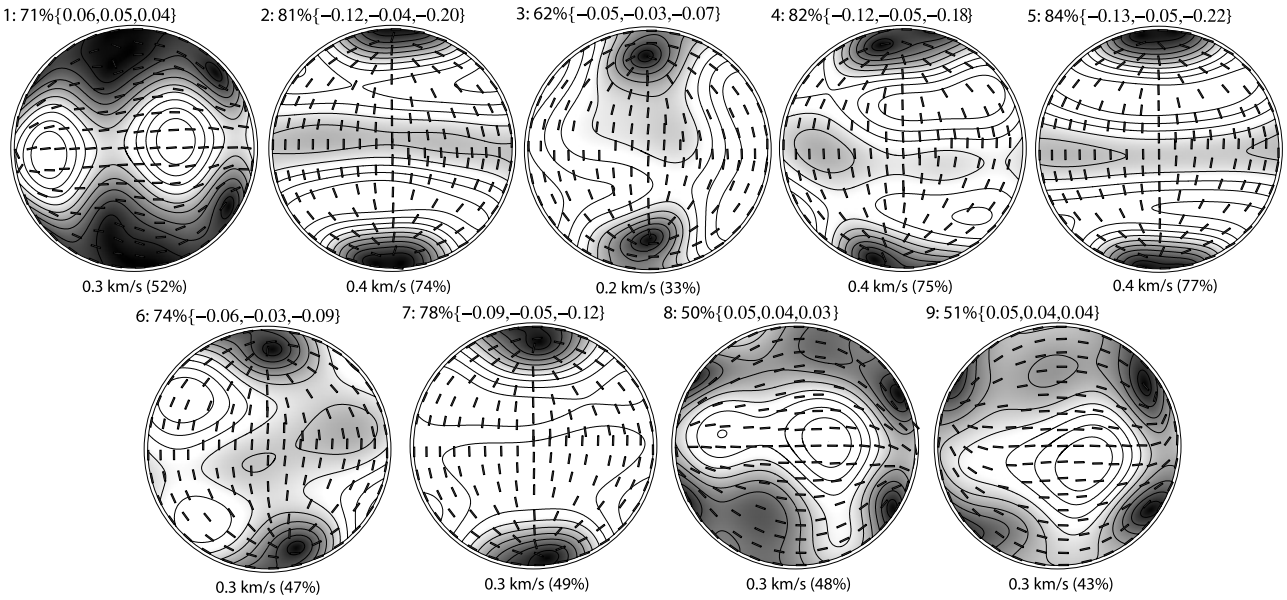

Figure 5. Predicted shear wave velocity anomaly based on best fit, hexagonal-symmetry oriented model tensors for the nine type localities of Figure 3 (see Appendix B and compare Figure B1). Note prediction of slow symmetry axes and strong nonhexagonal anisotropy component for samples 1, 8, and 9, as observed for some natural samples in Figure B1.

Δv_S surfaces as explained in Appendix B. Regions with large horizontal shear (e.g., underneath the Pacific plate, samples 4 and 5 in Figure 5) produce strong hexagonal anisotropy (anisotropy strengths are ~75% of the SC, ~80% of which is hexagonal). This gross behavior is, of course, not surprising, as such alignment of *a* axes is the basis of any of the geodynamic modeling attempts for A-type slip systems [e.g., *McKenzie*, 1979; *Nicolas and Christensen*, 1987; *Mainprice and Silver*, 1993; *Mainprice et al.*, 2000]. However, the more detailed match is reassuring. It implies that LPO development theories such as those of *Kaminski and Ribe* [2001], which are fit to laboratory experiments, lead to fabrics which are seen in natural samples (e.g., IM-SPR in Figure B1) when incorporated in geodynamic models. If the regular, hexagonal-type samples such as 2 and 5 were representative for a layer traversed by an *S* wave, the observed shear wave splitting would be similar to that of an ol/en SC. However, significant back-azimuth dependence of splitting may be observed if the TI axis is dipping out of the horizontal (this is masked by the rotated Δv_S plots of Figure 5).

[28] Interestingly, some samples (3 from the Sunda trench, 6 from a spreading ridge) show minor variations of the hexagonally dominated patterns that are also found in natural samples, or sample averages (IM-SUB and JI-CAS in Figure B1). Furthermore, we also find synthetic examples of slow symmetry axes (1 from East Africa, 8 from a regional upwelling underneath the western United States, and 9 from the North Atlantic ridge, Figures 3 and 5), where velocity gradients have a uniaxial compression component during transition from vertical upwelling to horizontal shearing. Such transition fabrics have lower hexagonal symmetry (~50%), and lower overall Δv_S amplitudes (~50% of SC). These more complex *C* tensors as imaged by Δv_S also exist in natural samples, IM-KIM, JI-ALL, and JI-NUN (Figure B1). There are several complicating factors (e.g., compositional effects) that need to be addressed. However, the match between model and natural LPO implies that the variety of LPOs observed in xenoliths may indeed be related to A-type deformation within upper mantle convection [cf. *Tommasi et al.*, 1999]. This is consistent with findings from geodynamic and field studies [e.g., *Ben Ismail and Mainprice*, 1998; *Mehl et al.*, 2003]. Complications due to high water/stress deformation [*Jung and Karato*, 2001; *Mizukami et al.*, 2004], or high melt content [*Holtzman et al.*, 2003], may be only of regional relevance [cf. *Kneller et al.*, 2005; *Lassak et al.*, 2006].

3.2.4. Global Character of Anisotropy

[29] Figure 6 shows the global distribution of predicted seismic anisotropy strength in terms of symmetry component tensor norms for the $\xi_c = 2$ reference flow model at 200 km depth. The average values of the *C* components at each layer are a convolution of the depth dependence of the SC properties (Figure 1) and the shear strain rates (Figure 2) via tracer paths. The mean and RMS variations of the tensor norm anisotropy are 7.2 ± 2.7% and 8.8 ± 1.3% for 100 and 300 km depth, respectively. At these depths, the hexagonal component makes up 5.4 ± 2.4% and 7.4 ± 1.3%, respectively. Therefore globally the hexagonal approximation for seismic anisotropy captures most (~80%) of the total anisotropy. It is only in certain regions (Figures 6b and 6c) where other anisotropy components become important. As Figure 6 shows, regions of strong vertical flow (e.g., East Pacific Rise) are locations of diminished anisotropy strength, and of nonhexagonal complexity. Both effects are due to strong reshaping of LPO along streamlines with transitions between different types of deformation regimes. Anisotropy strength patterns for models with lateral viscosity variations are similar to those depicted in Figure 6, but

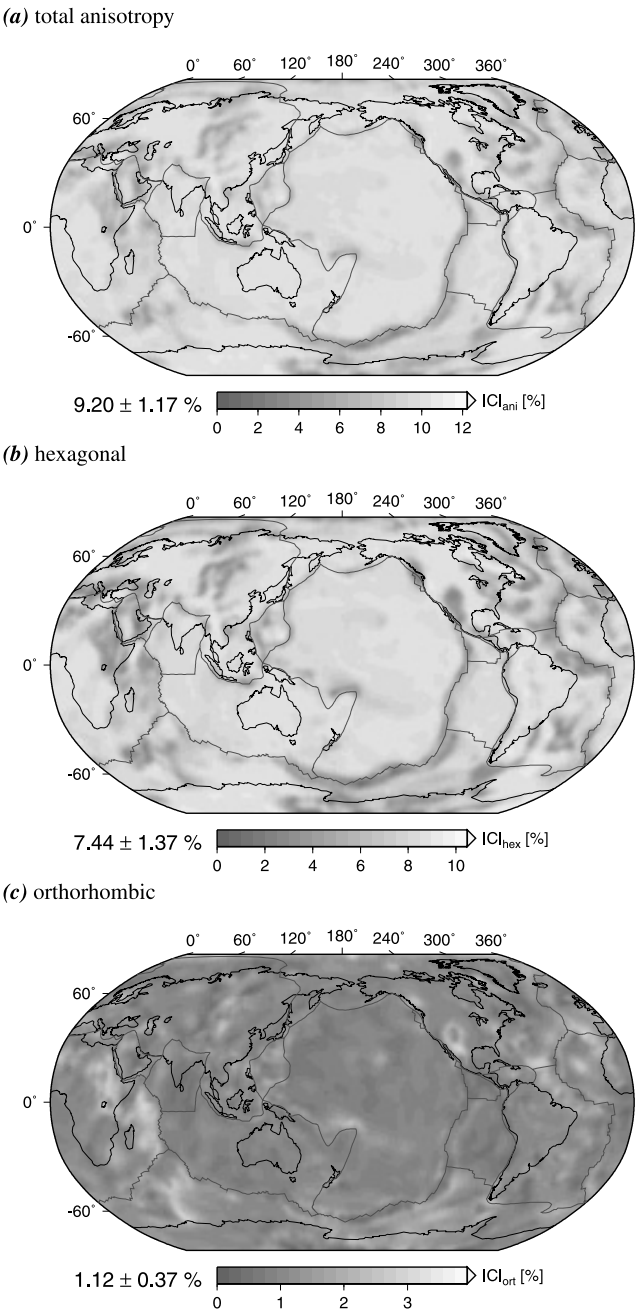

Figure 6. Predicted seismic anisotropy (symmetry tensor fractions, in % of total tensor norm) at 200 km depth for the reference flow model (ξ_c = 2, $\eta_D(z)$, compare Figure 3): (a) total anisotropy, (b) hexagonal approximation, and (c) orthorhombic symmetry components. Percentage value and ± range next to each scale bar denotes the mean and RMS variation. Note scale changes between Figures 6a, 6b, and 6c; color bars are clipped at 60% of the maximum.

the lateral fluctuations in strength in the regions of strong radial flow are weakened.

3.2.5. Correlation Relationships for Hexagonal Anisotropy

[30] After these general considerations, we last return to our goal of establishing correlation relationships for parameters ε, γ, and δ (i.e., correlation surfaces in the 3-D ε, γ, and δ space, equations (3)–(5)). Figure 7 shows the distribution of these hexagonal anisotropy parameters at 200 km depth in analogy to Figure 6. It is evident that *S* wave anisotropy, γ, is strongly correlated with *P* wave anisotropy, ε. This is true even more so for the ellipticity parameter, δ, and Figure 8 shows why. We display scatter diagrams for the reference model's γ and δ parameters versus ε for globally distributed synthetic samples, obtained from 50 to 300 km depths in 50 km spacing. The "data points" were generated by a roughly even area sampling at each layer ($\sim$4100 points each) of the global anisotropy models as shown in Figures 3, 6, and 7.

[31] Figure 8 compares the correlation relationship between the hexagonal parameters in $\{\varepsilon, \gamma, \delta\}$ space for simple shear experiments and *Kaminski et al.* [2004] type LPO formation with those obtained from our reference geodynamic model. Upper mantle convection apparently distributes tracers dominantly along the straining trend from randomly oriented LPO (no anisotropy) at {0, 0, 0} to the other end-member, perfect SC alignment (maximum anisotropy) denoted by inverted triangles (Figure 8). Naturally, ε is then also correlated with the total or hexagonal anisotropy strength, as shown in Figures 6b and 6c. The diamond symbols plotted on top of the shearing trend allow identification of a corresponding ξ strain relative to random LPO. If further calibrated using natural samples, such a relationship might be used as a strain gauge based on anisotropy measurements.

[32] Figure 8b also shows that the slope of the ε–δ relationship is not unity. This implies that $\varepsilon - \delta \neq 0$ in general, casting doubt on seismological studies that use this simplification of elliptical anisotropy. In addition to the straining trend, variations in the hexagonal correlations are caused by variations in velocity gradients due to tracer advection, as was discussed above. Further variations from the mixing trend arise due to changes in the SC elasticity tensors with ambient conditions (*p*, *T*). The strength of such effects is indicated by the two different trends from the SC symbols in Figure 8 based on *Estey and Douglas* [1986] or the set of newer parameters.

[33] To further illustrate the uncertainties in our synthetic anisotropy models, we show two different ways of performing the assemblage average for SC tensors, indicated by open and filled inverted triangles for the Reuss and Voigt end-member cases, respectively. Both *p*, *T* derivatives and assemblage averaging are thus not negligible factors, and details of the results may be affected by our choices. However, we also superimpose the natural samples of mantle rocks from Figure B1 on the synthetics in Figure 8 and observe encouraging consistency. This overall match between natural and synthetic fabric components may be exploited further, and it will be worthwhile to fine tune our geodynamic models (e.g., ξ_c and KR parameters) based on a larger number of individual and properly converted natural fabrics in future work.

[34] To explore the potential role of uncommon slip systems [*Jung and Karato*, 2001; *Katayama et al.*, 2004], we indicate where elastic tensors from olivine laboratory experiments (I. Katayama and S.-I. Karato, Effect of temperature on the B- to C-type olivine fabric transition and implications for flow pattern in the subduction zone, submitted to *Earth and Planetary Science Letters*, 2005, hereinafter referred to as Katayama and Karato, submitted

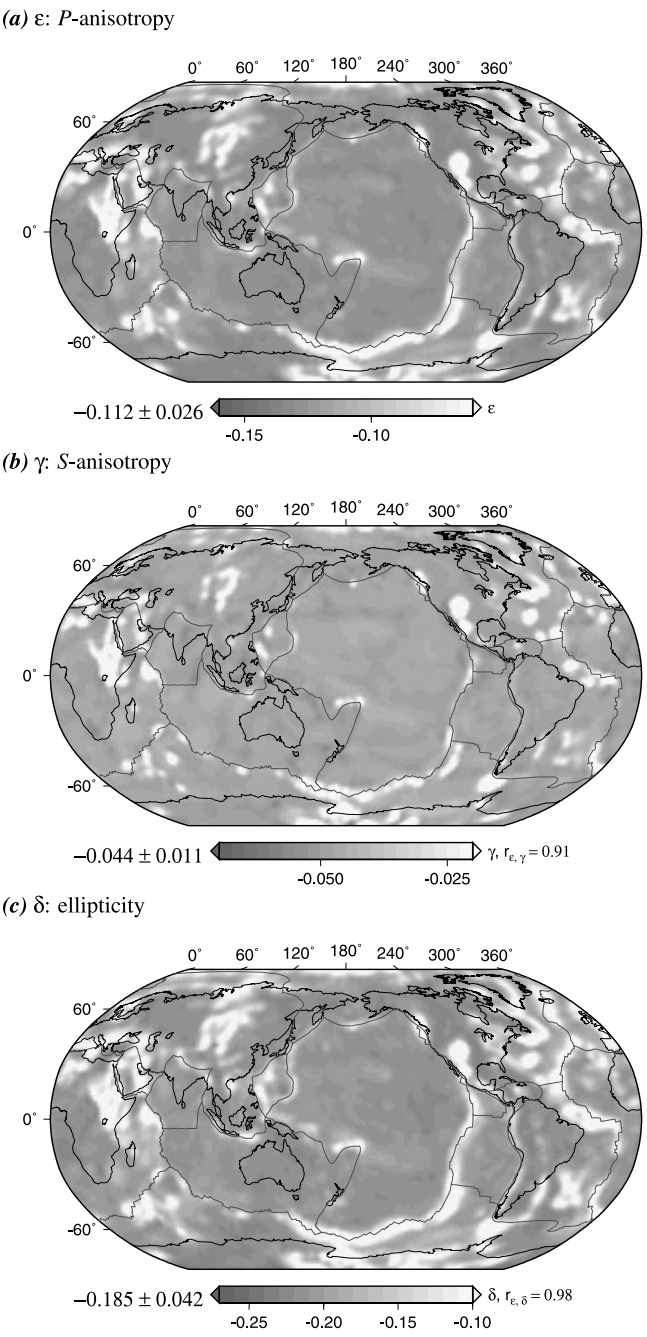

Figure 7. Hexagonal anisotropy parameters at 200 km for the reference model shown in Figure 6. (a) P wave anisotropy (ε), (b) S wave anisotropy (γ), and (c) ellipticity parameter (δ) (equations (3)–(5)). Values next to scale bars (spanning mean plus/minus two RMS for each plot) denote global mean plus/minus RMS variation, and labels on right for Figures 7b and 7c specify the linear correlation coefficient between ε and the respective parameter, e.g., r_{ε}, δ for the correlation between ε and δ.

manuscript, 2005) would plot in $\{\varepsilon, \gamma, \delta\}$ space. Their C tensors were computed by VRH averaging of a 100% olivine SC assemblage derived from the observed crystallographic axes at p = 5 GPa and T = 1573°K conditions (provided by I. Katayama, personal communication, August 2005). Ironically, the A-type deformation sample plots furthest outside the main trend in $\{\varepsilon, \gamma\}$ space. This could be for a number of reasons, including laboratory conditions, but such deviations should only be further evaluated by comparing olivine assemblages with identical dC/dp and dC/dT SC values, p, T conditions, averaging schemes. While these caveats also apply to the comparison with the natural samples, we cannot remedy these limitations at present, as we do not have all the required data available to us. However, as Figure 8 shows, the deviations of both laboratory and natural samples from the main trends are not that large, given the range of uncertainties. This implies that it may be impossible to detect uncommon slip system LPO fabrics based on anisotropy strength ratios. However, they would, of course, show up as local regions of modified fast propagation azimuths.

[35] Encouraged by the match between natural samples and synthetics, we proceed to analyze the $\{\varepsilon, \gamma, \delta\}$ scatter quantitatively. We performed a principal component analysis (PCA), which transforms the data into a new coordinate system as defined by eigenvector analysis. Ideally, most of the variance in the data can then be explained with a single, projected principal component. The PCA finds $\{-0.49, -0.15, -0.86\}$ as the principal eigenvector, $\mathbf{p}_1$, for the synthetics from the reference flow model in Figure 8. When the scatter is projected into $\mathbf{p}_1$, the projection coordinate, p_1, in PCA space renders a sharper image of the lateral variations of Figures 6 and 7, with maximum values within the highly sheared regions. Minima of p_1 are found in the regions of small anisotropy and large nonhexagonal components, e.g., within the radial flow domains. Only using $\mathbf{p}_1$ corresponds to fitting a linear relationship to the scatter of Figure 8. This projection leads to a variance reduction of the synthetics of 85%. Using the second eigenvector, $\mathbf{p}_2$ = $\{-0.50, -0.76, 0.42\}$, in addition to $\mathbf{p}_1$ allows capturing the second-order variations, particularly the small ε, γ anticorrelation with δ, better. Using p_1 and p_2, the variance reduction is almost complete at 97% (correspondingly, the PCA eigenvalue for $\mathbf{p}_2$ is only 2% of the eigenvalue for $\mathbf{p}_1$).

[36] We have evaluated several ways of fitting the scatter in Figure 8. However, given the uncertainties in SC C and our incomplete understanding of the robustness of the geodynamic models, e.g., with respect to viscosity variations, we think that no formal statistical analysis is warranted. Instead, we visually identified end-members for a bilinear fit. These relationships are denoted by dashed lines in Figure 8 and are as follows for γ:

$$\begin{aligned}\gamma &\approx -0.023(\pm 0.0120)\\ &\quad +0.233(\pm 0.07)\varepsilon \quad \varepsilon \le -0.03\\ \gamma &\approx -0.003(\pm 0.0006)\\ &\quad +0.900(\pm 0.10)\varepsilon \quad \varepsilon > -0.03,\end{aligned} \tag{8}$$

and for δ:

$$\begin{aligned}\delta &\approx 0.027(\pm 0.003)\\ &\quad +1.857(\pm 0.04)\varepsilon \quad \text{for} \quad \varepsilon \le -0.03\\ \delta &\approx 0.003(\pm 0.010)\\ &\quad +0.667(\pm 0.06)\varepsilon \quad \text{for} \quad \varepsilon > -0.03.\end{aligned} \tag{9}$$

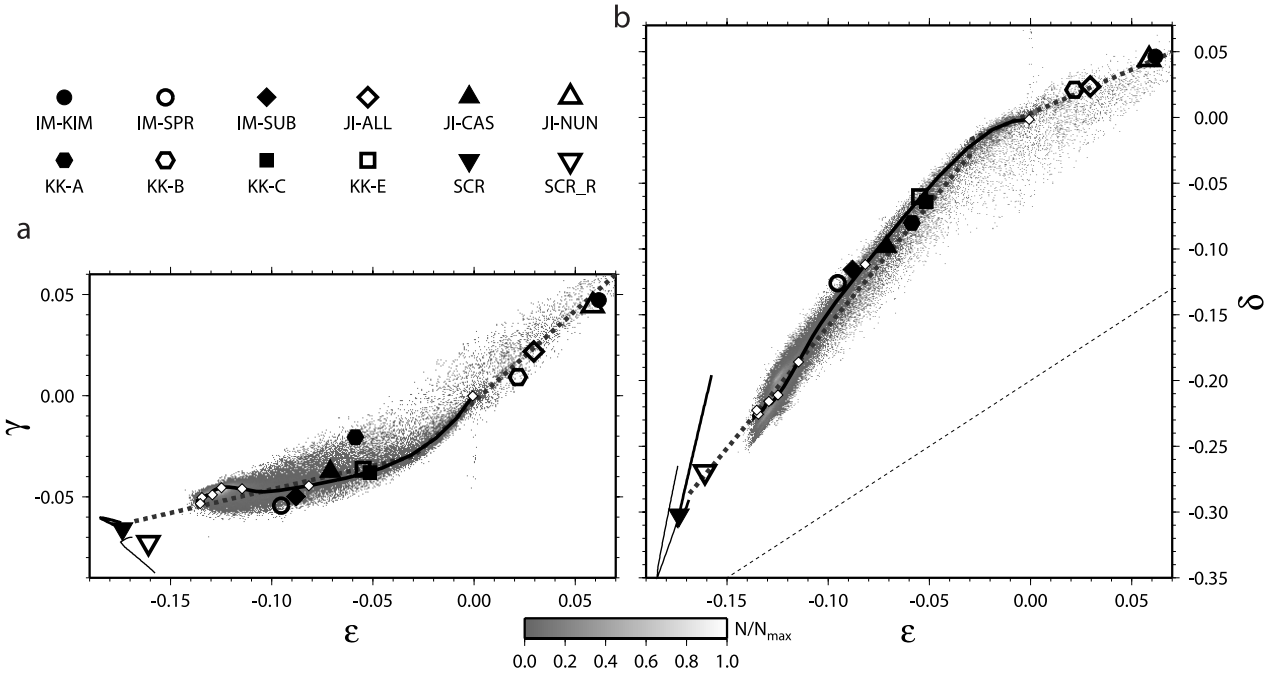

Figure 8. Hexagonal anisotropy factor correlations. Comparison of geodynamic synthetics (summed in background, based on sampling the reference model at 100, 200, and 300 km depth; shading normalized by maximum bin count) compared with natural samples (see Figure B1 for legend and references), laboratory-strained samples: KK-A, KK-B, KK-C, KK-E, A-, B-, C-, and E-type slip system samples after deformation [*Jung and Karato*, 2001; *Katayama et al.*, 2004; Katayama and Karato, submitted manuscript, 2005], and SC ol/en mix at RTP for Voigt (SCR) and Reuss (SCR_R) averaging. The thick and thin lines originating from the SC end-members denote the p, T dependence of a Voigt-averaged SC assemblage for the upper 410 km of the mantle using *Estey and Douglas* [1986] (as in the geodynamic model) or the more recent estimated of C derivatives, respectively (see text). Solid lines originating at zero anisotropy ($\{\varepsilon, \gamma, \delta\} = \{0, 0, 0\}$) denote predicted LPO anisotropy of a ol/en aggregate under simple shear using the *Kaminski et al.* [2004] theory (wiggles at high anisotropy are due to grain boundary sliding), white diamond symbols are plotted at every $\xi = 0.5$ increment. Dashed heavy lines denote our best fit, bilinear interpolation, based on visual inspection of the plots. Dotted line in Figure 8b denotes a unity slope relationship between ε and δ, as expected for elliptical anisotropy where $\varepsilon - \delta = 0$.

[37] Our physical interpretation of these bilinear relationships is that they correspond to approximations to the progressive LPO accumulation trends by means of simple shearing (solid line in Figure 8 toward negative $\{\varepsilon, \gamma, \delta\}$) and uniaxial compression (toward positive values). For the $\varepsilon - \gamma$ fit, our selection of the small ε end-member was guided by the C uncertainties and the SC location rather than the cluster of synthetic data, which would have led to slightly higher predictions for the $\varepsilon < -0.03$ line. Such considerations are more straightforward for the ε-δ fit. The uncertainties indicated by ±signs in equations (8) and (9) were estimated by comparing different fitting approaches, formal variances of a straight-line fit are much smaller.

[38] While there are slight variations in scatter/model fit with depth (see also Figure 1c), we do not think those are significant. Using the bilinear fit, we compute an average misfit for predicted γ of $\Delta_\gamma \approx 0.0044$ (assuming no error in ε), and for δ of $\Delta_\delta \approx 0.0075$ using the synthetics of Figure 8. Other geodynamic model synthetics for $\xi_c = 2$ show very similar data distributions, for instance when different radial viscosity profiles (e.g., that proposed by *Steinberger* [2000]) are used, or with regard to $\eta(T)$ or $\eta(T, \dot{\varepsilon})$ circulation models. For lateral viscosity contrasts, some of the extreme outliers of Figure 8 disappear, though average misfits are increased slightly to $\Delta\gamma \approx 0.005$ and $\Delta\delta \approx 0.009$ for both $\eta(T)$ and $\eta(T, \dot{\varepsilon})$. However, if we use shorter advection times and saturations strains, e.g., $\xi_c = 0.5$, the synthetics do not span the whole range of observations from laboratory samples as shown in Figure 8. Rather, anisotropy strengths are confined to $-0.1 \lesssim \varepsilon \lesssim 0.025$ and numerical and visual misfits with the bilinear (or hyperbolic resp. polynomial) trends in Figure 8 increase. We take this as an indication that large $\xi_c \sim 2$ are required to be able to invoke mantle convection as the main origin of the observed variations in natural samples.

[39] This robustness with regard to the geodynamic model assumptions confirms that tectonic flow details lead to second-order variations in addition to the dominant, progressive straining trend seen in Figure 8. We suggest using these relationships to simplify inversions of seismic anisotropy. The best fit equations (8) and (9) may be expected to capture upper mantle LPO anisotropy based

on insights from geodynamic modeling, as well as laboratory and field measurements.

4. Conclusions

[40] We constructed global geodynamic and mineral physics models for LPO anisotropy in the upper mantle. A comparison of best fit hexagonal anisotropy from full elasticity tensors with simpler FSE-derived models shows good agreement. This result confirms earlier conclusions that seismic anisotropy may be used as a constraint for mantle flow. Moreover, when using the [*Kaminski and Ribe*, 2001; *Kaminski et al.*, 2004] approach, the statistical properties of the predicted anisotropic fabrics resemble those of natural samples. This result should stimulate further, more careful study of global and regional applications. If confirmed, our findings imply that roughly the right ingredients (active slip systems and mineral physics theory) have been established to model LPO anisotropy at the global scale. Laboratory studies of LPO development may indeed translate into natural settings.

[41] Simple straining trend relationships between hexagonal anisotropic parameters appear to hold across different geodynamic models, and the synthetic $\{\varepsilon, \gamma, \delta\}$ ranges match those from natural samples at saturation strains of $\xi_c \sim 2$. Such correlations are thus consistent with range of observations and may allow future seismological studies to reduce the number of independent parameters dramatically for studies of seismic anisotropy. In general, the assumption of hexagonal symmetry applies to large extent over wide regions, with exceptions in certain tectonic settings. Different types of natural LPO fabrics may be related to different geodynamic environments, encouraging further quantitative study of the complex history of mantle rocks.

Appendix A: Additional Circulation Models Tested

[42] To evaluate flow models with lateral viscosity contrasts, we also employ the 3-D, spherical finite element (FE) code CitcomS, slightly modified from *Zhong et al.* [2000] and *Moresi and Solomatov* [1995] as provided by geoframework.org. With this, well bench marked, FE method, we can explore lateral viscosity variations and global power law creep mantle flow in the framework of anisotropy studies [*Becker et al.*, 2004]. In the main text, we discuss a few models where lateral viscosity variations, $\eta(T, \dot{\varepsilon})$, were inferred from temperature, T, as scaled from tomography, and convective flow including power law strain rate tensor, $\dot{\varepsilon}$, dependency. We use a simplified constitutive law [e.g., *Christensen*, 1984; *Zhong et al.*, 2000]:

$$\eta(z, T, \dot{\varepsilon}) = B(z)\eta_0(z)\dot{\varepsilon}_{II}^{\frac{1}{n}-1} \exp\left[\frac{E}{n}(T_c - T)\right], \qquad \text{(A1)}$$

where η_0 is the radial viscosity profile, T_c is the nondimensional reference temperature (0.5), T the scaled temperature as based on the tomographic model, $\dot{\varepsilon}_{II}$ is the second (shear) strain rate tensor invariant, E scales the strength of the temperature effect, and n is the power law exponent. B is a constant adjusted for each layer such that the laterally log-averaged viscosity is roughly equal for radially varying (η; $E = 0$, $n = 1$), temperature dependent ($\eta(T)$; $E = 30$, $n = 1$), and temperature and strain rate-dependent ($\eta(T, \dot{\varepsilon})$; $E = 30$, $n = 3$) cases. We limit η to vary only from 10^{17} to 10^{24} Pa s. Implicitly, $\eta(\dot{\varepsilon})$ variations are also limited because both the imposed strain rates due to plate motion variations across boundaries and due to density anomalies are quite small given the moderate model resolutions employed. The model rheology is not realistic for the Earth if laboratory studies are extrapolated [e.g., *Ranalli*, 1995], and composite creep laws [e.g., *McNamara et al.*, 2003] with larger viscosity variations provide a more realistic description. However, our intent here is to use these $\eta(T, \dot{\varepsilon})$ models to illustrate some of the effects of lateral viscosity contrasts on flow-derived anisotropy. We use 49,152 elements laterally, 65 elements radially, and iterate power law viscosity solutions until the incremental change in RMS velocities is below 3% of the total RMS velocity. We were able to reproduce $\{E = 0, n = 1\}$ [*Hager and O'Connell*, 1981] solutions with that FE resolution within a few percent velocity difference. With our R scaling, equation (A1) leads to moderate lateral variations of η based on temperature ($n = 1$), over $\sim$2 orders of magnitude at $\sim$400 km depth. We note that power law flow computations are demanding in terms of required resolution and are just beginning to be explored. A comprehensive study in 3-D spherical geometry akin to the study by *Christensen* [1984] is still missing, and we will not attempt it here.

[43] Lateral viscosity variations are required to produce net motion of the entire lithosphere as observed in a hot spot reference frame [*Ricard et al.*, 1991; *O'Connell et al.*, 1991; *Bercovici*, 2003]. We prescribe surface plate velocities in a no-net-rotation reference frame nonetheless, for consistency with [*Becker et al.*, 2003]. Also, initial tests performed with a prescribed net shear in the upper $\sim$250 km of the mantle (based on *Zhong* [2001]) led to a deterioration of the model fit to azimuthal anisotropy from surface waves. Using the FE formulation, we also computed circulation models with a free-slip top mechanical boundary condition and prescribed weak zones along the present-day plate boundaries [cf. *Zhong et al.*, 2000]. Without any fine tuning, such models reproduced surface RMS velocities to within $\sim$10%; velocity fields had correlation coefficients of $\sim$0.85. This finding confirms that the circulation models are dynamically consistent in terms of driving forces, as expected [*Becker and O'Connell*, 2001].

[44] The deformation mechanism leading to LPO anisotropy is dislocation creep, which may be expected to dominate the high stress, relatively low-temperature regime of the uppermost mantle [e.g., *Karato*, 1998]. All geodynamic models that model anisotropy for a specific region of the Earth have been based on Newtonian (linear, diffusion creep) rheologies to date, however. This is fundamentally inconsistent as diffusion creep would erase LPO fabrics. The argument has typically been that power law flow may look similar to Newtonian flow on large scales, but this assumption has not been thoroughly tested with global models. Recently, general models have been constructed using composite rheologies to study the transition between the two creep regimes and resulting anisotropy [*McNamara et al.*, 2002; *Podolefsky et al.*, 2004], and we have begun to explore power law rheologies in regional and

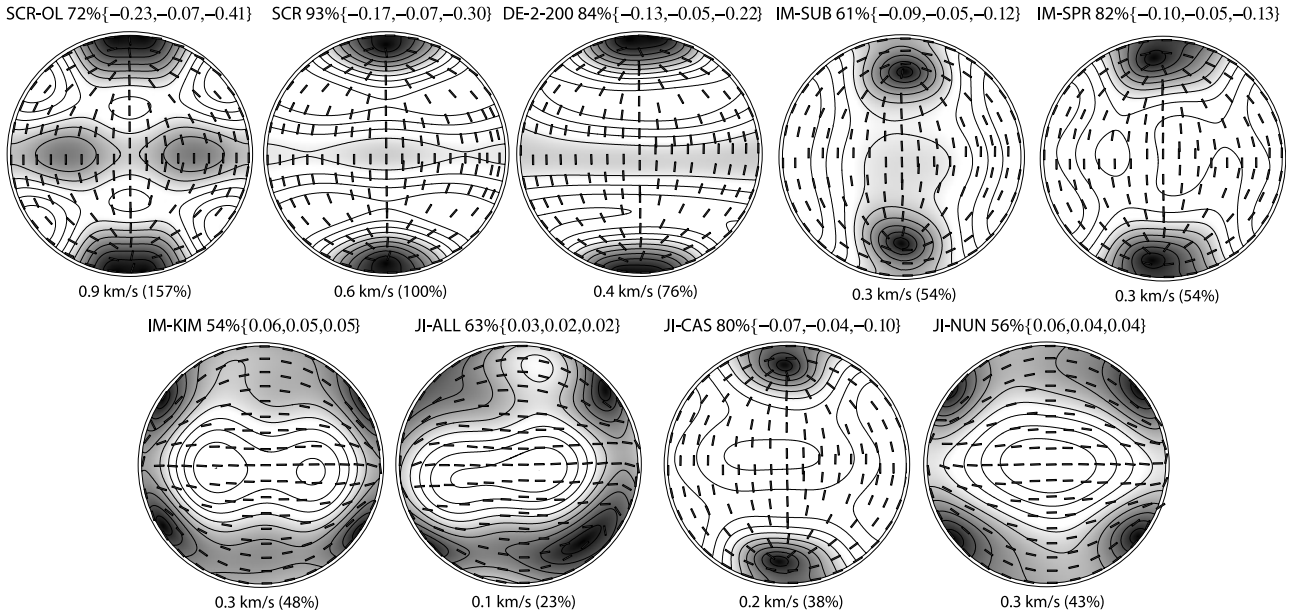

Figure B1. Shear wave anisotropy surfaces for elastic tensors from natural samples. Background shading shows Δv_S (equation (B1)), as a function of back azimuth (up is north, right is east) and incidence (center pole is vertical), upper hemisphere equal-area projection. Tensors were aligned so that the best fit (H_1) and worst fit (H_3) hexagonal symmetry axes point north and east, respectively. Anomalies are normalized by the maximum Δv_S for each plot (value and fraction of ol:en SC labeled below each subplot; for reference, SCR, $\Delta v_S \approx 0.58$ km/s). Contour interval 0.1 interval; bright colors show larger anomalies. Sticks indicate the propagation plane for the fast shear wave. Text above subplots indicate hexagonal anisotropy fraction relative to total and ε, γ, and δ factors (equations (3)–(5)). We show results for SC lab measurements, a straining test using the methods of this study, and natural samples. SCR-OL, olivine SC at room p, T (RTP); SCR, ol/en assemblage at RTP, Voigt averaged (flow alignment); DE-2-200, simple shear deformation experiment using the *Kaminski et al.* [2004] method and $\xi = 2$, at p, T for 200 km (all SC C from *Estey and Douglas* [1986]); IM-KIM, IM-SPR, IM-SUB, kimberlite, spreading ridge, and subduction setting sample averages, respectively, from *Ben Ismail and Mainprice* [1998]. JI-ALL, JI-CAS, JI-NUN, xenoliths samples from *Ji et al.* [1994].

global models. We found that regionally, the effect on modifying flow fields was moderate [*Becker et al.*, 2004] when compared to uncertainties in the density structure of the mantle. However, the thorough evaluation of the robustness of these findings is still needed. For most of our models here, we use linear creep, but assume that the corresponding LPO is formed by dislocation creep which is active everywhere above 410 km. Our models are therefore likely to produce an upper bound on the strength of anisotropy, as fabrics might be frozen in at shallow depth [cf. *Becker*, 2002]. Moreover, diffusion creep might be partly erasing anisotropic fabrics even in the upper mantle, and dominant slip systems might change at higher pressures [*Mainprice et al.*, 2005].

Appendix B: Benchmark Test of LPO Development and Comparison to Natural Samples

[45] In order to benchmark the KR algorithm in global flow models and to gain a general understanding of LPO formation, we conducted several simple deformation experiments for fabric development. We use the *Kaminski et al.* [2004] method and an ol/en assemblage under simple and pure shear, as well as uniaxial compression. Results are similar to those shown by, e.g., *Browaeys and Chevrot* [2004] and *Lassak et al.* [2006]. For simple shear, a randomly aligned assemblage develops LPO such that the elastic anisotropy increases roughly exponentially first, then starts to level off at $\xi \sim 0.7$, and reaches fairly constant, asymptotic values between $\xi \sim 1.5$ and 2. For such strained samples at $\xi = 3$, the total, hexagonal, and orthorhombic tensor anisotropy fractions are ~11, 9, and 1%, respectively (rest 0.6%), using *Estey and Douglas* [1986] SC values at 200 km depth ($T = 1810°$ K and $p = 6.4$ MPa) and Voigt averaging. Without grain boundary sliding, values are higher, ~14, 12, and 1%. Best fit TI orientations are normally stable before anisotropy and LPO saturates, within $\xi \sim 0.5$ and 1. The development of LPO and anisotropy symmetries is similar for other deformation experiments, though we find more fluctuations for $\xi \gtrsim 2$ around the asymptotic values for pure shear, or uniaxial compression. If we consider preexisting LPO, we find that a large amount of additional straining of $\xi \sim 1.5$ and 2 is typically needed to reorient the fast axes TI orientations by 90° [cf. *Kaminski and Ribe*, 2002]. The finding that it is harder to reorient existing fabrics is consistent with experiments by *Lassak et al.* [2006] for A- to B-type slip system transitions. Saturation values, ξ_c, are thus larger than those expected from earlier theories for LPO [*Ribe*, 1992]. *Ribe*'s [1992] work and best fit model considerations led us to use $\xi_c \sim 0.5$

before [*Becker et al.*, 2003], though we found that models were not very sensitive to ξ_c. However, we are now faced with the possible requirement to advect for longer times if we want to ensure that the most recent deformation episode has overprinted whatever texture might have preexisted. This reemphasizes the fact that time-dependent convection scenarios should be considered carefully in the next phase of this research.

[46] LPO fabrics can be visualized with pole figures showing the orientation distributions for the three crystallographic axes of the individual mineral grains (e.g., Figure 4). Adding a step of interpretation, seismic wave speed anomalies can be computed from an averaged elasticity tensor [e.g., *Mainprice et al.*, 2000]. While this step involves the aforementioned uncertainties regarding SC elasticity constants and averaging methods, it is more intuitive for geodynamic interpretation. We use the standard Christoffel matrix approach (see, e.g., *Schulte-Pelkum and Blackman* [2003] for details) and either a fixed reference density of 3353 kg/m^3 for lab samples, or PREM derived densities for model elasticity tensors. Figure B1 shows shear wave anisotropy surfaces for SCs, a KR straining experiment, and several xenolith samples from the literature. We orient all C tensors along the best fit hexagonal axis (symmetry Cartesian coordinate system of *Browaeys and Chevrot* [2004]) and show the Δv_S anisotropy

$$\Delta v_s = v_{S1} - v_{S2} \tag{B1}$$

as well as the local fast propagation planes as a function of back azimuth and incidence. When referring to relative Δv_S anisotropy amplitudes, we shall use

$$\delta v_S = \frac{\Delta v_S}{\bar{v}_S} = 2\frac{v_{S1} - v_{S2}}{v_{S1} + v_{S2}}. \tag{B2}$$

[47] As is well known (e.g., discussion by *Blackman et al.* [2002]), the orthorhombic component of the olivine SC anisotropy (SCR-OL in Figure B1) is partly suppressed by the addition of enstatite (SCR), so that the Δv_S surface is more symmetrical. The simple shear LPO-produced tensor (DE-2-200) leads to Δv_S anomalies that are ~80% of the perfectly aligned SC values at $\xi = 2$. Natural samples in Figure B1 were plotted based on published C tensors, most often estimated from VRH averaging. The samples show only some similarity to the predominantly hexagonal Δv_S pattern expected from simple deformation histories of an ol/en assemblage. This is not surprising given their slightly different mineral composition, and presumably more complex tectonic deformation histories. Most fabrics show fast best fit hexagonal symmetry axes, with ε, γ, $\delta < 0$. The Δv_S anisotropy amplitudes of the natural samples are ~ a third smaller than strained samples at $\xi = 2$; fast propagation azimuths are more similar between lab and natural samples. IM-KIM, JI-ALL, and JI-NUN are different from the typical hexagonally dominated LPOs. Their fabrics show slow hexagonal symmetry, as indicated by positive ε, γ, and δ values and $\gamma \approx \delta$. Such types of LPOs form under uniaxial compression (where a axes align in a girdle around the compressive axis [e.g., *Nicolas et al.*, 1973]) and are observed to have a stronger orthorhombic component than the regular fabrics with ε, $\gamma < 0$. In general, anisotropy amplitudes are 20–55% of the SC Δv_S, and the hexagonal fraction is between ~50 and 80% for the natural samples of Figure B1.

[48] **Acknowledgments.** We thank A. McNamara and an anonymous reviewer for their constructive comments; J. Browaeys for discussion of tensor decompositions; E. Kaminski for providing and helping with D-REX; H. Schmeling for comments on this code and LPO fabrics; A. McNamara, J. van Hunen, and E. Tan for help with Citcom; S. Zhong, L. Moresi, M. Gurnis, and others involved in the geoframework.org effort for sharing Citcom; J. B. Kellogg, R. J. O'Connell, and B. Steinberger for their earlier support of this project; and I. Katayama and D. Mainprice for sharing a preprint and averaged elasticity tensor data. T.W.B. was supported by NSF grants EAR-0330717 and EAR-0409373, and computation for the work described in this paper was supported by the University of Southern California Center for High Performance Computing and Communications (http://www.usc.edu/hpcc). Most figures were produced with the GMT software by *Wessel and Smith* [1991].

References

Abramson, E. H., J. M. Brown, L. J. Slutsky, and J. Zaug (1997), The elastic constants of San Carlos olivine up to 17 GPa, *J. Geophys. Res.*, *102*, 12,253–12,263.

Anderson, D. L., and A. M. Dziewoński (1982), Upper mantle anisotropy: Evidence from free oscillations, *Geophys. J. R. Astron. Soc.*, *69*, 383–404.

Barruol, G., and H. Kern (1996), P and S wave velocities and shear wave splitting in the lower crustal/upper mantle transition (Ivrea zone): Experimental and calculated data, *Phys. Earth Planet. Inter.*, *95*, 175–194.

Becker, T. W. (2002), Lithosphere–mantle interactions, Ph.D. thesis, Harvard Univ., Cambridge, Mass.

Becker, T., and L. Boschi (2002), A comparison of tomographic and geodynamic mantle models, *Geochem. Geophys. Geosyst.*, *3*(1), 1003, doi:10.1029/2001GC000168.

Becker, T. W., and R. J. O'Connell (2001), Predicting plate velocities with mantle circulation models, *Geochem. Geophys. Geosyst.*, *2*(12), doi:10.1029/2001GC000171.

Becker, T. W., J. B. Kellogg, G. Ekström, and R. J. O'Connell (2003), Comparison of azimuthal seismic anisotropy from surface waves and finite-strain from global mantle-circulation models, *Geophys. J. Int.*, *155*, 696–714.

Becker, T. W., D. K. Blackman, and V. Schulte-Pelkum (2004), Seismic anisotropy in the western US as a testbed for advancing combined models of upper mantle geodynamics and texturing (abstract), *Eos Trans. AGU*, *85*(47), Fall Meet. Suppl., Abstract T33A-1338.

Becker, T. W., V. Schulte-Pelkum, D. K. Blackman, J. B. Kellogg, and R. J. O'Connell (2006), Mantle flow under the western United States from shear wave splitting, *Earth Planet. Sci. Lett.*, *247*, 235–251.

Behn, M. D., C. P. Conrad, and P. G. Silver (2004), Detection of upper mantle flow associated with the African Superplume, *Earth Planet. Sci. Lett.*, *224*, 259–274.

Ben Ismail, W., and D. Mainprice (1998), An olivine fabric database: An overview of upper mantle fabrics and seismic anisotropy, *Tectonophysics*, *296*, 145–157.

Bercovici, D. (2003), The generation of plate tectonics from mantle convection, *Earth Planet. Sci. Lett.*, *205*, 107–121.

Blackman, D. K., and J.-M. Kendall (2002), Seismic anisotropy in the upper mantle: 2. Predictions for current plate boundary flow models, *Geochem. Geophys. Geosyst.*, *3*(9), 8602, doi:10.1029/2001GC000247.

Blackman, D. K., H.-R. Wenk, and J. M. Kendall (2002), Seismic anisotropy of the upper mantle: 1. Factors that affect mineral texture and effective elastic properties, *Geochem. Geophys. Geosyst.*, *3*(9), 8601, doi:10.1029/2001GC000248.

Boschi, L., and G. Ekström (2002), New images of the Earth's upper mantle from measurements of surface wave phase velocity anomalies, *J. Geophys. Res.*, *107*(B4), 2059, doi:10.1029/2000JB000059.

Browaeys, J., and S. Chevrot (2004), Decomposition of the elastic tensor and geophysical applications, *Geophys. J. Int.*, *159*, 667–678.

Čadek, O. (2005), Constraints on global mantle-flow models from geophysical data (abstract), in *9th International Workshop on Numerical Modeling of Mantle Convection and Lithospheric Dynamics*, *Int. Sch. Geophys.*, vol. 25, edited by E. Boschi, pp. 15–16, Ettore Majorana Found. and Centre for Sci. Culture, Erice, Sicily, Italy.

Chai, M., J. M. Brown, and L. J. Slutsky (1997), The elastic constants of an aluminous orthopyroxene to 12.5 GPa, *J. Geophys. Res.*, *102*, 14,779–14,785.

Chastel, Y. B., P. R. Dawson, H.-R. Wenk, and K. Bennett (1993), Anisotropic convection with implications for the upper mantle, *J. Geophys. Res.*, *98*, 17,757–17,771.

Christensen, U. R. (1984), Convection with pressure- and temperature-dependent non-Newtonian rheology, *Geophys. J. R. Astron. Soc.*, *77*, 343–384.

Dziewoski, A. M., and D. L. Anderson (1981), Preliminary reference Earth model, *Phys. Earth Planet. Inter.*, *25*, 297–356.

Ekström, G. (2001), Mapping azimuthal anisotropy of intermediate-period surface waves (abstract), *Eos Trans. AGU*, *82*(47), Fall Meet. Suppl., Abstract S51E-06.

Estey, L. H., and B. J. Douglas (1986), Upper mantle anisotropy: A preliminary model, *J. Geophys. Res.*, *91*, 11,393–11,406.

Favier, N., and S. Chevrot (2003), Sensitivity kernels for shear wave splitting in transverse isotropic media, *Geophys. J. Int.*, *153*, 213–228.

Forsyth, D. W. (1975), The early structural evolution and anisotropy of the oceanic upper mantle, *Geophys. J. R. Astron. Soc.*, *43*, 103–162.

Fouch, M. J., P. G. Silver, D. R. Bell, and J. N. Lee (2004), Small-scale variations in seismic anisotropy near Kimberley, South Africa, *Geophys. J. Int.*, *157*, 764–774.

Gaboret, C., A. M. Forte, and J.-P. Montagner (2003), The unique dynamics of the Pacific hemisphere mantle and its signature on seismic anisotropy, *Earth Planet. Sci. Lett.*, *208*, 219–233.

Hager, B. H., and R. W. Clayton (1989), Constraints on the structure of mantle convection using seismic observations, flow models, and the geoid, in *Mantle Convection: Plate Tectonics and Global Dynamics*, *Fluid Mech. Astrophys. Geophys.*, vol. 4, edited by W. R. Peltier, pp. 657–763, Gordon and Breach, New York.

Hager, B. H., and R. J. O'Connell (1981), A simple global model of plate dynamics and mantle convection, *J. Geophys. Res.*, *86*, 4843–4867.

Hall, C. E., K. M. Fischer, E. M. Parmentier, and D. K. Blackman (2000), The influence of plate motions on three-dimensional back arc mantle flow and shear wave splitting, *J. Geophys. Res.*, *105*, 28,009–28,033.

Hess, H. H. (1964), Seismic anisotropy of the uppermost mantle under oceans, *Nature*, *203*, 629–631.

Holtzman, B. K., D. L. Kohlstedt, M. E. Zimmerman, F. Heidelbach, T. Hiraga, and J. Hustoft (2003), Melt segregation and strain partitioning: Implications for seismic anisotropy and mantle flow, *Science*, *301*, 1227–1230.

Isaak, D. G. (1992), High-temperature elasticity of iron-bearing olivines, *J. Geophys. Res.*, *97*, 1871–1885.

Ji, S., X. Zhao, and D. Francis (1994), Calibration of shear-wave splitting in the subcontinental upper mantle beneath active orogenic belts using ultramafic xenoliths from the Canadian Cordillera and Alaska, *Tectonophysics*, *239*, 1–27.

Jung, H., and S.-I. Karato (2001), Water-induced fabric transitions in olivine, *Science*, *293*, 1460–1463.

Kaminski, É., and N. M. Ribe (2001), A kinematic model for recrystallization and texture development in olivine polycrystals, *Earth Planet. Sci. Lett.*, *189*, 253–267.

Kaminski, É., and N. M. Ribe (2002), Timescales for the evolution of seismic anisotropy in mantle flow, *Geochem. Geophys. Geosyst.*, *3*(8), 1051, doi:10.1029/2001GC000222.

Kaminski, É., N. M. Ribe, and J. T. Browaeys (2004), D-Rex, a program for calculation of seismic anisotropy due to crystal lattice preferred orientation in the convective upper mantle, *Geophys. J. Int.*, *157*, 1–9.

Karato, S.-I. (1992), On the Lehmann discontinuity, *Geophys. Res. Lett.*, *51*, 2255–2258.

Karato, S.-I. (1998), Seismic anisotropy in the deep mantle, boundary layers and the geometry of convection, *Pure Appl. Geophys.*, *151*, 565–587.

Katayama, I., H. Jung, and S.-I. Karato (2004), New type of olivine fabric from deformation experiments at modest water content and low stress, *Geology*, *32*, 1045–1048.

Kneller, E. A., P. E. van Keken, S.-I. Karato, and J. Park (2005), B-type olivine fabric in the mantle wedge: Insights from high-resolution non-Newtonian subduction zone models, *Earth Planet. Sci. Lett.*, *237*, 781–797.

Laske, G., and G. Masters (1998), Surface-wave polarization data and global anisotropic structure, *Geophys. J. Int.*, *132*, 508–520.

Lassak, T. M., M. J. Fouch, C. E. Hall, and E. Kaminski (2006), Seismic characterization of mantle flow in subduction systems: Can we resolve a hydrated mantle wedge?, *Earth Planet. Sci. Lett.*, *243*, 632–649.

Love, A. E. H. (1927), *A Treatise on the Mathematical Theory of Elasticity*, Cambridge Univ. Press, New York.

Mainprice, D., and P. G. Silver (1993), Interpretation of *SKS*-waves using samples from the subcontinental mantle, *Phys. Earth Planet. Inter.*, *78*, 257–280.

Mainprice, D., G. Barruol, and W. Ben Ismail (2000), The seimic anisotropy of the Earth's mantle: From single crystal to polycrystal, in *Earth's Deep Interior: Mineral Physics and Tomography From the Atomic to the Global Scale*, *Geophys. Monogr. Ser.*, vol. 117, edited by S.-I. Karato et al., pp. 237–264, AGU, Washington, D. C.

Mainprice, D., A. Tommasi, H. Couvy, P. Cordier, and N. J. J. Frost (2005), Pressure sensitivity of olivine slip systems and seismic anisotropy of Earth's upper mantle, *Nature*, *433*, 731–733.

McKenzie, D. P. (1979), Finite deformation during fluid flow, *Geophys. J. R. Astron. Soc.*, *58*, 689–715.

McNamara, A. K., P. E. van Keken, and S.-I. Karato (2002), Development of anisotropic structure in the Earth's lower mantle by solid-state convection, *Nature*, *416*, 310–314.

McNamara, A. K., P. E. van Keken, and S. Karato (2003), Development of finite strain in the convecting lower mantle and its implications for seismic anisotropy, *J. Geophys. Res.*, *108*(B5), 2230, doi:10.1029/2002JB001970.

Mehl, L., B. R. Hacker, G. Hirth, and P. B. Kelemen (2003), Arc-parallel flow within the mantle wedge: Evidence from the accreted Talkeetna arc, south central Alaska, *J. Geophys. Res.*, *108*(B8), 2375, doi:10.1029/2002JB002233.

Mizukami, T., S. R. Wallis, and J. Yamamoto (2004), Natural examples of olivine lattice preferred orientation patterns with a flow-normal a-axis maximum, *Nature*, *427*, 432–436.

Montagner, J. P., and D. L. Anderson (1989), Petrological constraints on seismic anisotropy, *Phys. Earth Planet. Inter.*, *54*, 82–105.

Montagner, J.-P., and L. Guillot (2000), Seismic anisotropy in the Earth's mantle, in *Problems in Geophysics for the New Millenium*, edited by E. Boschi, G. Ekström, and A. Morelli, pp. 217–253, Compositori, Bologna, Italy.

Montagner, J. P., and H. C. Nataf (1988), Vectorial tomography - I. Theory, *Geophys. J.*, *94*, 295–307.

Montagner, J.-P., and T. Tanimoto (1991), Global upper mantle tomography of seismic velocities and anisotropies, *J. Geophys. Res.*, *96*, 20,337–20,351.

Montagner, J.-P., D.-A. Griot-Pommera, and J. Laveé (2000), How to relate body wave and surface wave anisotropy?, *J. Geophys. Res.*, *105*, 19,015–19,027.

Moresi, L., and V. S. Solomatov (1995), Numerical investigations of 2D convection with extremely large viscosity variations, *Phys. Fluids*, *7*, 2154–2162.

Nataf, H.-C., and Y. Ricard (1996), 3SMAC: An a prior tomographic model of the upper mantle based on geophysical modeling, *Phys. Earth Planet. Inter.*, *95*, 101–122.

Nicolas, A., and N. I. Christensen (1987), Formation of anisotropy in upper mantle peridotites: A review, in *Composition, Structure and Dynamics of the Lithosphere-Asthenosphere System*, *Geodyn. Ser.*, vol. 16, edited by K. Fuchs and C. Froidevaux, pp. 111–123, AGU, Washington, D. C.

Nicolas, A., F. Boudier, and A. M. Bouillier (1973), Mechanisms of flow in naturally and experimentally deformed peridotites, *Am. J. Seismol.*, *273*, 853–876.

Niehuus, K., and H. Schmeling (2005), Temporal geoid variations as constraint in global geodynamics, in *9th International Workshop on Numerical Modeling of Mantle Convection and Lithospheric Dynamics*, *Int. Sch. Geophys.*, vol. 36, edited by E. Boschi, pp. 15–16, Ettore Majorana Found. and Centre for Sci. Culture, Erice, Sicily, Italy.

O'Connell, R. J., C. W. Gable, and B. H. Hager (1991), Toroidal-poloidal partitioning of lithospheric plate motions, in *Glacial Isostasy, Sea-Level and Mantle Rheology*, edited by R. Sabadini, pp. 535–551, Springer, New York.

Podolefsky, N. S., S. Zhong, and A. K. McNamara (2004), The anisotropic and rheological strcuture of the oceanic upper mantle from a simple model of plate shear, *Geophys. J. Int.*, *158*, 287–296.

Ranalli, G. (1995), *Rheology of the Earth*, 2nd ed., CRC Press, Boca Raton, Fla.

Reuss, A. (1929), Berechnung der Fliegrenze von Mischkristallen auf Grund der Plastizitätsbedingung für Einkristalle, *Z. Angew. Math. Mech.*, *9*, 49–58.

Ribe, N. M. (1989), Seismic anisotropy and mantle flow, *J. Geophys. Res.*, *94*, 4213–4223.

Ribe, N. M. (1992), On the relation between seismic anisotropy and finite strain, *J. Geophys. Res.*, *97*, 8737–8747.

Ribe, N. M., and Y. Yu (1991), A theory for plastic deformation and textural evolution of olivine polycrystals, *J. Geophys. Res.*, *96*, 8325–8335.

Ricard, Y., C. Doglioni, and R. Sabadini (1991), Differential rotation between lithosphere and mantle: A consequence of lateral mantle viscosity variations, *J. Geophys. Res.*, *96*, 8407–8415.

Rümpker, G., and P. G. Silver (1998), Apparent shear-wave splitting parameters in the presence of vertically varying anisotropy, *Geophys. J. Int.*, *135*, 790–800.

Russo, R. M., and P. G. Silver (1994), Trench-parallel flow beneath the Nazca plate from seismic anisotropy, *Science*, *263*, 1105–1111.

Saltzer, R. L., J. B. Gaherty, and T. H. Jordan (2000), How are vertical shear wave splitting measurements affected by variations in the orientation of azimuthal anisotropy with depth?, *Geophys. J. Int.*, *141*, 374–390.

Savage, M. K. (1999), Seismic anisotropy and mantle deformation: What have we learned from shear wave splitting?, *Rev. Geophys.*, *37*, 65–106.

Schulte-Pelkum, V. (2001), Mantle structure and anisotropy from the particle motion and slowness of compressional body waves, Ph.D. thesis, University of Calif., San Diego, La Jolla.

Schulte-Pelkum, V., and D. K. Blackman (2003), A synthesis of seismic *P* and *S* anisotropy, *Geophys. J. Int.*, *154*, 166–178.

Silver, P. G. (1996), Seismic anisotropy beneath the continents: Probing the depths of geology, *Annu. Rev. Earth Planet. Sci.*, *24*, 385–432.

Silver, P. G., and W. E. Holt (2002), The mantle flow field beneath western North America, *Science*, *295*, 1054–1057.

Simons, F. J., and R. D. van der Hilst (2003), Seismic and mechanical anisotropy and the past and present deformation of the Australian lithosphere, *Earth Planet. Sci. Lett.*, *211*, 271–286.

Stacey, F. D. (1977), A thermal model of the Earth, *Phys. Earth Planet. Inter.*, *15*, 341–348.

Steinberger, B. (2000), Plumes in a convecting mantle: Models and observations for individual hotspots, *J. Geophys. Res.*, *105*, 11,127–11,152.

Tanimoto, T., and D. L. Anderson (1985), Lateral heterogeneity and azimuthal anisotropy of the upper mantle: Love and Rayleigh waves 100–250 s, *J. Geophys. Res.*, *90*, 1842–1858.

Tommasi, A. (1998), Forward modeling of the development of seismic anisotropy in the upper mantle, *Earth Planet. Sci. Lett.*, *160*, 1–13.

Tommasi, A., B. Tikoff, and A. Vauchez (1999), Upper mantle tectonics: Three-dimensional deformation, crystallographic fabrics and seismic properties, *Earth Planet. Sci. Lett.*, *168*, 173–186.

Tommasi, A., D. Mainprice, G. Canova, and Y. Chastel (2000), Viscoplastic self-consistent and equilibrium-based modelling of olivine lattice preferred orientation: 1. Implications for the upper mantle seismic anisotropy, *J. Geophys. Res.*, *105*, 7893–7908.

Vinnik, L. P., V. Farra, and B. Romanowicz (1989), Azimuthal anisotropy in the Earth from observations of *SKS* at Geoscope and Nars broadband stations, *Bull. Seismol. Soc. Am.*, *79*, 1542–1558.

Voigt, W. (1928), *Lehrbuch der Kristallphysik*, Teuber, Berlin, Germany.

Wenk, H.-R., and C. N. Tomé (1999), Modeling dynamic recrystallization of olivine aggregates deformed in simple shear, *J. Geophys. Res.*, *104*, 25,513–25,527.

Wenk, H.-R., K. Bennett, G. R. Canova, and A. Molinari (1991), Modelling plastic deformation of peridotite with the self-consistent theory, *J. Geophys. Res.*, *96*, 8337–8349.

Wessel, P., and W. H. F. Smith (1991), Free software helps map and display data, *Eos Trans. AGU*, *72*, 445–446, 441.

Zhang, S., and S.-I. Karato (1995), Lattice preferred orientation of olivine aggregates deformed in simple shear, *Nature*, *375*, 774–777.

Zhang, S., S.-I. Karato, J. F. Gerald, U. H. Faul, and Y. Zhou (2000), Simple shear deformation of olivine aggregates, *Tectonophysics*, *316*, 133–152.

Zhong, S. (2001), Role of ocean-continent contrast and continental keels on plate motion, net rotation of lithosphere, and the geoid, *J. Geophys. Res.*, *106*, 703–712.

Zhong, S., M. T. Zuber, L. Moresi, and M. Gurnis (2000), Role of temperature-dependent viscosity and surface plates in spherical shell models of mantle convection, *J. Geophys. Res.*, *105*, 11,063–11,082.

T. W. Becker, Department of Earth Sciences, University of Southern California, MC0740, Los Angeles, CA 90089-0740, USA. (twb@usc.edu)

D. K. Blackman, IGPP, Scripps Institution of Oceanography, University of California, San Diego, La Jolla, CA 92093-0225, USA.

S. Chevrot, Laboratoire de Dynamique Terrestre et Planétaire, Observatoire Midi Pyrénées Université Paul Sabatier, F-31400 Toulouse, France.

V. Schulte-Pelkum, CIRES, Department of Geological Sciences, Boulder, CO 80309-0399, USA.